Forcing-dependent submesoscale variability and subduction in a coastal sea area (Gulf of Finland, Baltic Sea)

Kai Salm, Germo Väli, Taavi Liblik, and Urmas Lips

Department of Marine Systems, Tallinn University of Technology, Tallinn, Estonia.

5 Correspondence to: Kai Salm (Kai.Salm@taltech.ee)

Abstract. Submesoscale (SMS) processes withinin a stratified coastal environment are characterized based onof the Gulf of Finland (Baltic Sea) were investigated using glider missions and a realistic simulation with the SMS permitting agrid spacing of 0.125 nautical miles. The study period covered the conditions of the transition from developing and to established seasonal stratification in the Gulf of Finland (Baltic Sea). The tracer variance maximum was detected. SMS variability, defined as smallscale anomalies of temperature and salinity cancelling each other's contribution to density (spice), was concentrated around the base of the upper mixed layer (UML) depth and shallower than the depth of the maximum density gradient in spring and inwithin the seasonal thermocline in late summer. We suggest that atmospheric forcing is the key driver of these disparities. In spring and early summer, predominantly positive net this shift was caused by the changes in surface heat flux promoted water column stratification, and wind-induced mixing often did not reach the lower portion forcing. Both observations and simulations revealed events of the UML likely high SMS flows due to the horizontal buoyancy gradients developed there. In conditions, when the net surface heat flux was close to zero or negative, variability, which can be related to background mesoscale dynamics and changes in wind forcing-had a more prominent role in shaping dynamics within the thermocline. High SMS tracer variance was consistently observed and simulated. We examined the event in which elevated spice in the subsurface layers at the layer did not coincide with the high Rossby number O(1) in the surface layer but instead appeared offshore side of a coastal baroclinic current-characterized by slanted, Sloping isopycnals, and intensified vertical velocities pointed to active SMS subduction. We propose that topography related frontal instabilities of frontal currents can create favourable conditions for SMS subduction transporting tracers from the sea., likely related to flow-topography interactions, drive the lateral and downward transport of surface near coastal boundary towards offshore and downwards, waters, contributing to tracer redistribution below the seasonal thermocline.

25 1 Introduction

Submesoscale (SMS) flows, occupying the intermediate horizontal scale of ~1 km (Taylor and Thompson, 2023), are increasingly recognized as critical drivers of vertical exchanges of heat, carbon, and nutrients in the upper ocean, with important implications for stratification, biogeochemical cycling, and ecosystem productivity (e.g., Mahadevan, 2016). These

processes bridge the energy transfer between larger, geostrophically balanced motions and microscale turbulence, making them central to upper-ocean dynamics (Capet et al., 2008; Naveira Garabato et al., 2022).

30

The ocean is a vast dynamic system that is constantly in motion, driven by forces, including winds, tides, and changes in density gradients due to temperature and salinity. As differences. These forces generate motion across a result, awide range of differentspatial scales of motion forms. In a common theoretical framework, from large-scale geostrophic currents to small-scale turbulent mixing. Traditionally, upper ocean's turbulence is dominated by thehas been understood as a combination of mesoscale quasi-geostrophic eddies, internal waves, and microscale three-dimensional turbulence, but recently the attention has been on the contribution of the submesoscale processes (e.g., Taylor and Thompson, 2023). The submesoscale (SMS) is recognized to transfer energy from the geostrophically near balanced flows to small-scale turbulence (Capet et al., Mesoscale dynamics, with 2008; Naveira Garabato et al., 2022).

At the mesoscale, i.e., characteristic horizontal sealescales of O(10–100) km in the ocean and O(5–20) km in the Baltic Sea, the flow is close to the geostrophic balance. Dynamically, mesoscale eddies are is characterized by small Rossby number $\left(Ro = \frac{u}{fL}, Ro \ll 1\right)$ and large Richardson number $\left(Ri = \frac{N^2H^2}{u^2}, Ri \gg 1\right)$, meaning reflecting dominance of rotational and buoyancy effects are strong in shaping fluid motion-forces (Taylor and Thompson, 2023). Here, U is a characteristic horizontal velocity scale, L and H are horizontal and vertical length scales, f is the Coriolis parameter, and N is the Brunt-Väisälä frequency. The In contrast, SMS occupies intermediate space scale of O(1) km and dynamics is characterized with by Ro O(1) and Ri-both in the order of O(1) (Thomas et al., 2008), meaning<1, indicating a dynamic regime where rotation, stratification, and inertia are all important to the SMS dynamics. Compared to the mesoscale, the Earth rotation does not constrain the motion to the same extent and thus, strong vertical motions can develop. The SMS processes effectively induce the vertical fluxes of heat, carbon and nutrients between the surface and the interior, making them relevant to phytoplankton productivity (Mahadevan, 2016 inertial forces all play important roles (Thomas et al., 2008). The weaker rotational constraint allows SMS processes to generate strong vertical velocities (e.g., Chrysagi, 2021; Tarry et al., 2022).

The Baltic Sea is aRecent advances in observational technology, particularly the use of autonomous gliders, have significantly improved our ability to detect SMS structures. With their high spatial resolution and adaptive sampling capabilities, gliders are well suited to capturing the smaller-scale variability associated with SMS processes. For example, Jhugroo et al. (2020) identified low-salinity SMS features driven by riverine input in a New Zealand shelf sea, which could intensify local stratification and displace a well-mixed surface layer up to 100 km offshore before being entrained by regional currents. Similarly, Bosse et al. (2021) used gliders to sample frontal zones in the northwestern Mediterranean Sea, revealing strong vertical motions and subduction events. In the Baltic Sea, studies such as by Carpenter et al. (2020) and Salm et al. (2023) have begun to reveal the role of SMS dynamics in shaping water column structure and vertical exchanges. However, given the region's complex stratification and ecological sensitivity, further glider-based studies are needed to resolve SMS processes and their biogeochemical implications in more detail.

This study focuses on the Gulf of Finland (GoF), an elongated sub-basin of the Baltic Sea – a semi-enclosed, brackish, shallow marginal sea in Northern Europe that stretches from 54° N to 66° N. The sea has limited water exchange with the North Sea, and the input of fresh river water is large. The Neva River, the largest river discharge is located freshwater source, discharges at the eastern end of the Gulf of Finland (GoF), a sub-basin in the northeastern Baltic Sea. The gulf is characterized by the pronounced horizontal salinity gradient, resulting from significant freshwater runoff at the eastern end of the gulf and the transport of Meanwhile, saltier water is transported into the gulf through its western border—, creating a pronounced horizontal salinity gradient across the gulf.

The flow field in the GoF, affectingwhich governs the freshwater transport and shapingshapes both horizontal and vertical salinity gradients, is significantly influenced by the wind (Lilover et al., 2017; Westerlund et al., 2019). For instance, in the case of prevailing Prevailing along-gulf winds, can establish a wind-driven circulation pattern, with currents along the wind near the coasts and in the opposite direction counter-flows in the central gulf can develop (Lips et al., 2017; Elken et al., 2011) that, as a result, enhances). These circulation patterns enhance transverse salinity gradients.

In contrast to the open ocean, the vertical salinity gradient has an equally important role alongside temperature in shaping the

density stratification of the water column in the GoF. In spring summer, a seasonal thermocline forms around depths of 10–30 meters, while below it and in the whole water column during the rest of the year, the salinity governs the vertical stratification Along. The quasi-permanent haloeline lies below 60 meters on average (Liblik and Lips, 2017). During winter and early spring, shallow haline stratification can develop because of freshwater advection (Liblik et al., 2020; Lips et al., 2017).

The along gulf winds favour the occurrence of also promote upwelling and downwelling events offalong the northern and southern coasts (Kikas and Lips, 2016; Lehmann et al., 2012). The summer upwelling events are typically associated with substantial temperature gradients at the sea surface (Lips et al., 2009; Uiboupin and Laanemets, 2009). Due), and due to the pronouncedstrong horizontal and vertical salinity gradients in the GoF and the development of jet currents along the upwelling fronts, also lead to pronounced salinity redistribution (Suursaar and Aps. 2007), upwelling events also alter the salinity distribution. By analysing the). Frontal structures and hydrographic variability and patterns associated with coastal upwelling serve as indicators of temperature and salinity distributions, one can estimate theenhanced vertical mixing (Lips et al., 2009) and the emergence of SMS activity features, such as filaments and eddies (Väli et al., 2017) associated with upwelling events.). During spring and summer, a seasonal thermocline typically forms at depths of 10-30 meters. Beneath this layer - and throughout the water column during the remainder of the year – vertical stratification is predominantly controlled by salinity. The quasi-permanent halocline lies below 60 meters on average (Liblik and Lips, 2017). In winter and early spring, shallow haline stratification can also develop because of freshwater advection (Liblik et al., 2020; Lips et al., 2017). The increasing number of studies analysing the captured SMS variability in the Baltic Sea supports the prevalence of the SMS processes (Carpenter et al., 2020; Lips et al., 2016a; Salm et al., 2023). Although the high resolution measurements gathered with autonomous devices offer insights into the water column structure, the analysis regarding the SMS from the observational data are limited. Therefore, complementing observations with numerical modelling yields supplementary data that enhance our

90

analytical capabilities and enables extrapolation of the findings in space and time. The models allow us to describe the background forcing and estimate the quantities indicative of the SMS regime that cannot be derived from the glider mission data alone. In this study, we aim to explore the role of SMS processes within a In the GoF, the vertical salinity gradient has an equally important role alongside temperature in shaping the density stratification of the water column, highlighting a key difference 100 from general open ocean conditions. Building on previous observational evidence of SMS features in the GoF (Salm et al., 2023), this study aims to further investigate the role of SMS processes in this stratified coastal environment, focusing on the upper half of the water column. Three glider missions were conducted in the GoF in spring summer 2018 2019, using a combination of observational and numerical tools. The appearance of SMS features favoured by associated with the development of a mesoscale front and 105 changing wind forcing was documented based on mission data from spring 2018 (Salm et al., 2023). We employHere, we extend the data of analysis to all three missions from conducted in the same area by analysing in spring summer 2018-2019. We examine tracer variability at the horizontal scale of a km. We compare the measurements with the simulation that has the SMS permitting grid spacing of 0.125 nautical miles (approximately 232 m) and use the model data to analyse the background forcing and dynamical properties, stratification, and coastal upwelling and downwelling events. Furthermore, model data allow 110 us to extrapolate the analysis over the whole spring summer season of both years, specifically spice, which represents temperature and salinity variations that compensate for each other in density (Rudnick & Cole, 2011). We propose that scalespecific spice at horizontal scales of a few kilometers can be used as an indicator of SMS activity, especially in conditions when temperature and salinity contribute comparably to density stratification. In the GoF, this is applicable in late spring and summer, when both thermal and haline stratification are significant. Although spice can potentially be advected over some 115 distance, the rapidly changing, wind-driven circulation in the GoF (Lilover et al., 2017) limits the transport of SMS features, thereby justifying a localized analysis. Ultimately, spice reveals anomalies and spatial gradients along isopycnals, where SMS processes often act. It serves as a proxy for SMS intensity capturing variability without being masked by vertical excursions of isopycnal surfaces, i.e., internal waves. We use spice—the temperature and salinity differences that cancel each other in the density—as a passive tracer and propose 120 that the scale dependent spice variance can be used as an indicator for the SMS dynamics (e.g., Rudnick and Cole, 2011). Spice can potentially be transported away from its source. However, with the high variability of the predominantly wind-driven current field in the GoF (Lilover et al., 2017) and the short-term nature of individual SMS features, this transport should be limited in space. Nevertheless, we relate the observed and modelled SMS variability to the conditions in a broader area to explain the emergence of high SMS spice variance at the background of mesoscale dynamics. Note also that using spice 125 variance as an indicator of SMS activity is applicable best if the variability in temperature and salinity contribute almost equally to the variability in density, which is not the case at low temperatures (from late autumn to early spring) in the brackish waters of the GoF.

We focus on the upper half of the water column, where SMS activity is most prominent and glider data are more densely sampled, allowing more robust analysis. Our study is limited to the spring-summer period, when seasonal stratification develops and becomes well established. This time window allows us to focus on our main objective of understanding SMS generation under stratified conditions.

To complement and expand upon glider observations, we employ a high-resolution numerical model with SMS-permitting horizontal grid spacing (~232 m), enabling us to characterize the dynamical background and infer SMS activity beyond the limited scope of *in situ* measurements. For meaningful SMS analysis, model data were averaged over a 10×10 km study window ("time series box"; 59.67–59.76° N, 25.06–25.25° E; see Fig. 1). This averaging accounts for the potential spatial and temporal displacement of SMS features, which are highly sensitive to small changes in initial conditions, model resolution, and parameterized processes. By situating glider observations within a wider model domain, the analysis accommodates these discrepancies and captures how background mesoscale conditions modulate SMS activity, thus enabling more robust interpretations of physical variability.

140 The following hypotheses are considered. We in this study. First, we suggest that the variations in the intensity of submesoscale features depend on varying SMS variability is modulated by both atmospheric forcing, particularly surface heat flux and wind stress, and the background (larger-scale) hydrographic conditions. Furthermorestructures, including mesoscale frontal gradients. Second, we propose that topography related topographically or forcing-induced instabilities of baroclinic coastal currents contribute to the vertical fluxescreate favourable conditions for SMS subduction, enabling offshore and downward transport of tracers through the seasonal thermocline. To test these hypotheses, we use glider data and high-resolution simulations to characterize temporal, vertical and horizontal distributions of SMS features and explore associated dynamical forcing. These complementary approaches allow us to link observed variability at the submesoscale with the underlying physical mechanisms and evaluate the role of SMS processes in stratified coastal environments.

The paper is organized as follows: Section 2 introduces the observations observational datasets, the numerical experiment, and the analysis methods; Section 3 provides presents the results, including the analysis of focusing on the spice variability and the SMS_permitting events; Section 4 discusses the presence of the SMS activity in the study area; the last section summarizes the work-implications of our findings for SMS activity in coastal stratified seas; Section 5 concludes with a summary of key results and their broader relevance.

2 Data and Methods

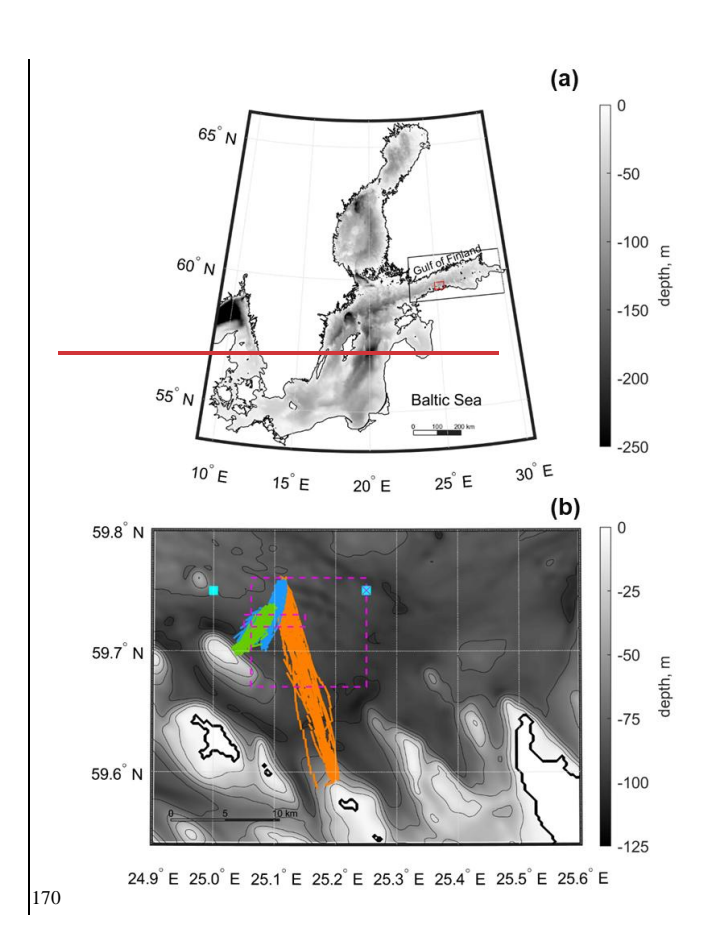
130

155 2.1 Glider observations

The study area is Although originally conducted for different research objectives, three glider missions in the GoF, Baltic Sea (Fig. 1). Missions were carried out in 1), collectively provide a dataset for this study. The field campaigns took place from 9 May—to 6 June 2018 and, from 21 May to 19 June 2019, and from 21 July—to 10 August 2019, during which an autonomous underwater vehicle, the Slocum G2 Glider MIA, collected oceanographic data along predefined transects. In May—June 2018,

an 18 km long transect was sampled 26 times, and in 2019, 4.5 and 5.5 km long-transects were each sampled over 90 times.

AltogetherIn total, over 12,000 profiles were gathered. These transects were oriented across the southern coast of the GoF, capturing cross-shore variability. The rawglider profiled the water column from the surface down to depths of 80–100 meters, depending on the position. While under the surface, the glider started to turn around either 4 m before the surface or 5–6 m before the seafloor. Raw data were quality controlled, and the coefficients to account following procedures adapted from Argo quality control protocols (Wong et al., 2025). Corrections for thesensor response time of the sensors and the thermal lag were definedapplied to minimize differences between two consecutive CTD profiles, similarly asfollowing the approach described by Salm et al. (2023). The half YOsUp- and downcasts were bin-averaged to a uniform 0.5 dbar vertical grid and arranged as profiles. For the analysis, the data fields were interpolated ononto a regular grid with a time step of 10 min, which was equalcorresponding to thean average horizontal distance of 130 m-on average.



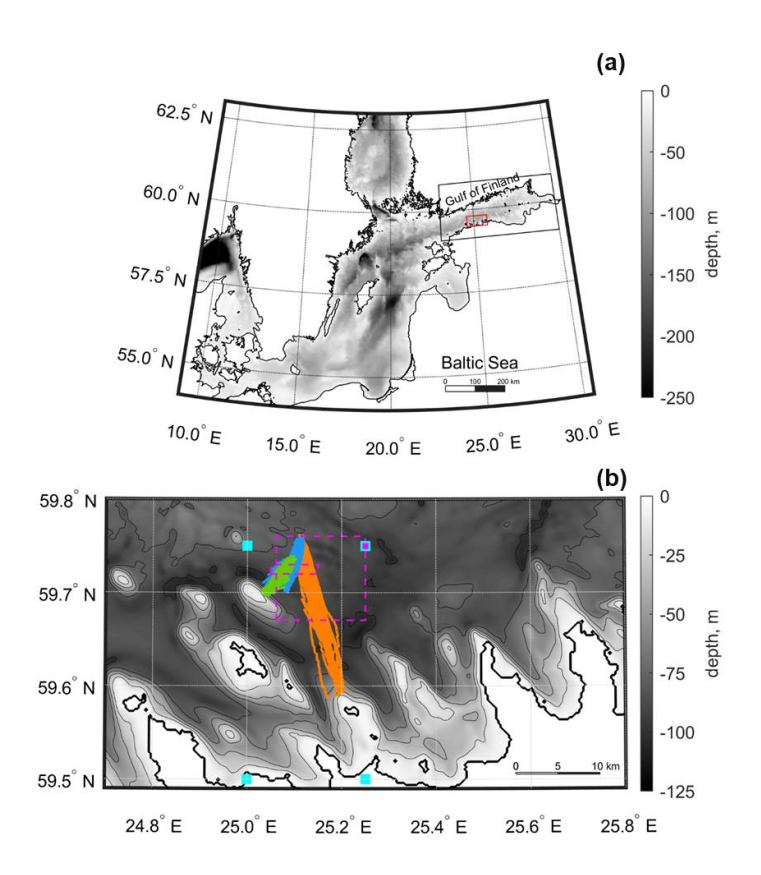


Figure 1: Map of (a) the Baltic Sea and (b) the study area. The red rectangle onin panel (a shows) indicates the location of the study area. The depth shown in panel (b). Depth isolines onin panel (b) are presentedshown with a step of 20 m. The glider (lifter missions carried out in from May-June 2018 and, May-June 2019, and July-August 2019 are shown in orange, blue, and green, respectively. The larger magenta box showsmarks the "time series box" chosen for the modelled data, and while the smaller one showsmagenta box indicates the area common area covered into all missions (59.72–59.73° N 25.05–25.15° E) and), used for the comparison of comparing glider and model data. The evan squares show the positions of the ERA5 grid points used for extracting the radiation data are shown by cyan squares, and the magenta cross the wind data; by the magenta square. The colormap shows the bathymetry used in the model.

180 **2.2 Model setup**

We are usingused a three-dimensional nested setup of the General Estuarine Transport Model (GETM; Burchard and Bolding, 2002) to simulate the circulation and the temperature and salinity distributiondistributions in the GoF. GETM is a primitive-

equation, free-surface, hydrostatic model with built-in vertically adaptive coordinates (Gräwe et al., 2015; Hofmeister et al., 2010; Klingbeil et al., 2018). Such a grid is a generalization of sigma layers with the potential to enhance vertical resolution near boundaries and in layers with strong stratification and shear (Klingbeil et al., 2018). Previous studies have shown that the total variation diminishing (TVD) advection scheme, combined with the superbee limiter, reduces the numerical mixing in the simulations (Gräwe et al., 2015; Klingbeil et al., 2018). Vertical mixing in the GETM iswas calculated by coupling it with the General Ocean Turbulence Model (GOTM; Umlauf and Burchard, 2005) and more). More precisely, we are using the twoequation k-\varepsilon turbulence model (Burchard and Bolding, 2001; Canuto et al., 2001) was used in the simulation.

The entire GoF iswas the high-resolution model domain, with a uniform horizontal grid spacing of 0.125 nautical miles (approximately 232 m) and 60 adaptive layers in the vertical. Original bathymetry was obtained from the EMODnet database (last accessed 09.06.2023) with a resolution of 1/16 arc minutes (approximately 150 m). Bathymetry data were averaged to the model resolution, and missing values were interpolated using the nearest neighbour (NN) technique.

The high-resolution simulation with an open western boundary at the GoF entrance was performed starting on 3 December 195 2017. The initial temperature and salinity fields and boundary conditions were taken from coarse-resolution simulations covering, respectively, the entire Baltic Sea with a grid step of 1 nautical mile (see Väli et al., 2024 for more details) and the Baltic Proper (including the GoF) with a grid step of 0.5 nautical miles (see Zhurbas et al., 2018 and Liblik et al., 2020, 2022 for more details). As all setups use adaptive coordinates, we first interpolated the profiles from the coarse-resolution model to thea fixed 5 m vertical resolution before spatial interpolation to the high-resolution model grid using the NN method. If needed, the profiles were extended to the bottom of the high-resolution grid to compensate for the bathymetric differences. The model run started from a motionless state with zero sea surface height and current components. Previous studies by Krauss and Brügge (1991) and Lips et al. (2016b) have shown that the spin-up time for the Baltic Sea model under atmospheric forcing is less than 10 days. For the boundary conditions, the temperature, salinity, and current profiles and the, as well as sea surface height, all with a 1-hour temporal resolution from the 0.5 nautical milesmile resolution simulation, were used. The same model setup was used by Siht et al. (in press2025), where further details and some-validation results are presented. Some quantitative information on model performance regarding stratification and SMS variability, which are the focus of the present paper, are given in subsection 3.1.

200

The atmospheric forcing at the sea surface (the momentum and heat flux) iswas calculated from the European Centre for Medium-Range Weather Forecasts atmospheric reanalysis data setdataset (ERA5, Hersbach et al., 2020) by utilizing wind components and other relevant parameters (air temperature, total cloudiness, relative humidity, sea level pressure) for bulk formulae by Kondo (1975). All meteorological parameters arewere interpolated bi-linearly to the model grid. The riverine freshwater input to the Baltic Sea was taken from the dataset produced for the Baltic Model Intercomparison Project (BMIP; Gröger et al., 2022) based on the E-HYPE (Lindström et al., 2010) hindcast and forecast products by Väli et al. (2019). There arewere 91 rivers in the dataset, of which 13 arewere in the GoF.

2.3 Submesoscale analysis

230

235

While air-sea fluxes, turbulent mixing, and advection introduce variability in the seawater properties, the dynamical processes act quickly to remove density differences. Spice – the <u>combination of</u> temperature and salinity <u>differences variations</u> that cancel each <u>other in other's contribution to</u> density – is the <u>traceresidual signal</u> that remains (Rudnick and Ferrari, 1999). Spice was defined as the sum of the temperature anomalies ΔT_z scaled by the thermal expansion coefficient α_z and the salinity anomalies.

 ΔS_{\perp} scaled by the haline contraction coefficient $\frac{(spice = \alpha \Delta T + \beta \Delta S)}{(spice = \alpha \Delta T + \beta \Delta S)}$, β_{\perp} as shown in Eq. (1):

the vertical sections of temperature and salinity distributions alone (Fig. 2b, c).

$$spice = \alpha \Delta T + \beta \Delta S. \tag{1}$$

The coefficients were calculated according to McDougall and Barker (2011). In this study, anomalies refer to the differences of between the measured or modelled Conservative Temperature or Absolute Salinity from the and their average value values along an isopycnal, calculated in theover a surrounding area of 4 km. For the observations, it was implemented as a moving window along the glider trajectory-and; for the model, it was computed over a 4×4 km square. The chosen length scale was chosen based onis consistent with the internal Rossby deformation radius in the GoF, which is typically 2–4 km in the GoF (Alenius et al., 2003).

We analysed the spice variance based on both the observations and the model results. The choice of a 4 km averaging scale offers a practical balance between resolving SMS structures and suppressing high-frequency noise. A smaller averaging scale may exaggerate variability and obscure persistent features, while a larger averaging scale poses a risk of smoothing out key SMS signals. Thus, 4 km averaging preserves the essential gradients and anomalies linked to SMS dynamics without compromising interpretability. Figure 2a shows an example of spice derived from the observations. The patches of positive (negative) spice indicate regions with higher salinitysalinities and warmer temperaturetemperatures (lower salinitysalinities and eolder temperaturetemperatures) compared to the average values in the surrounding 4 km- on the same isopycnal surface. Spice effectively highlights the smaller-scale (submesoscale SMS) variability that may be challenging to discern solely-from

The average spice intensity was defined as the root mean square of spice from the sea surface to the depth of minimum temperature. The UML depth was determined as the minimum depth where $\rho_z \ge \rho_{\overline{z}}\rho_3 + 0.25 \ kg \ m^{-3}$ was satisfied (ρ_z is the density at depth z and $\rho_1\rho_2$ at $\frac{1}{2}$ m). The strength and position of the pycnocline (we use, primarily associated with the term "upper pyenocline" (UP) for it)seasonal thermocline, were analysed based on the maximum of squared Brunt-Väisälä frequency (N²) and its corresponding depth. The vertical buoyancy gradient was estimated as $N^2 = b_{z_z}$, calculated over 2 m vertical intervals. Buoyancy was defined as Eq. (2):

For the model validation, we show that the development of stratification and tracer variability captured in the measurements is present in the simulation. The model data were averaged over a 1×1 km area, chosen inside a common area that was covered in all glider missions (59.72–59.73° N, 25.13–25.15° E, see Fig. 1). Considering submesoscale analysis, meaningful comparisons require averaging the model data over a 10×10 km study window, referred to as the "time series box" (59.67–59.76° N, 25.06–25.25° E; see Fig. 1), as features may be spatially and temporally displaced in the model.

The quantities $b = -\frac{g}{\rho_0}(\rho - \rho_0)_{a}$

(2)

250 where ρ_0 is the reference density of 1000 kg m⁻³.

Quantities indicative of the SMS regime, such as the Rossby number, (Ro), balanced Richardson number, (Ri), and horizontal buoyancy gradient, were calculated based on the model data. The Rossby number and the balanced Richardson number Ro and Ri were estimated, respectively, as Eq. ($\frac{43}{2}$):

$$Ro = \frac{\zeta}{f}$$
, $(\frac{13}{2})$

255 and Eq. (24):

265

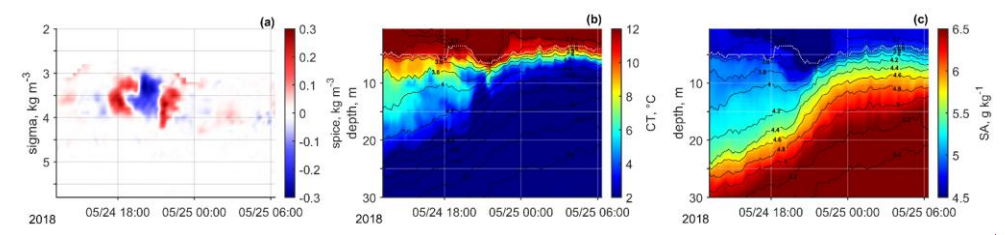
$$Ri = \frac{f^2 N^2}{|\nabla u b|^2}.$$
 (24)

 $\zeta = v_x - u_y$ is the vertical component of relative vorticity, f is the Coriolis frequency, $N^2 = b_z$ -vertical buoyancy gradient (squared Brunt Väisälä frequency)—and $|\nabla_H b| = \sqrt{b_x^2 + b_y^2}$ horizontal buoyancy gradient modulus. Centred finite-difference Buoyancy was defined as Eq. (3):

$$260 \quad b = -\frac{g}{\rho_0} (\rho - \rho_0)_{\bar{\tau}} \tag{3}$$

where $\rho_{\overline{q}}$ is the reference density of 1000 kg m⁻². Central scheme was used to calculate the parameters from the model. Horizontal and vertical steps for estimating gradients were 500 m and 2 m, respectively.

Wind data and parameters defining heat exchange between the atmosphere and the sea surface were extracted on the ERA5 product grid cells covering the study area (59.50–59.75° N, 25.00–25.25° E; see Fig. 1). The wind components in the analysis were smoothed by a Gaussian low-pass filter for 6 h to reduce high-frequency noise and highlight relevant forcing scales.



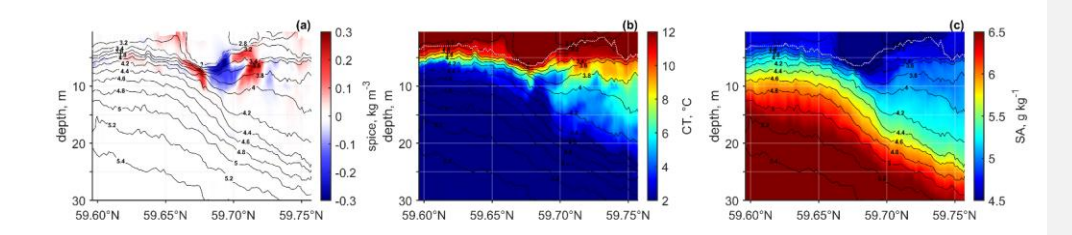


Figure 2: An example Example sections of (a) spice distribution (a) and , (b) temperature (b), and (c) salinity (e) sections with overlappedoverlaid density contours, based on glider data from 24–25 May 2018. The white dashed line shows indicates the upper mixed layer depth.

3 Results

275

290

3.1 Stratification and spice from observations and model

First, we compared model results with the observed vertical structureTo present temporal evolutions of the water column and tracer variability. A dataset equivalent to the glider measurements was extracted from the model's 30 minute output. Astratification and spice in the study area and enable direct comparison, we averaged both model and observational data over the same spatial region. We selected a common area covered in all missions was chosen (59.72–59.73° N 25.05–25.15° E, Fig. 1);) and averaged the consecutive profiles inside that area were averaged perwithin this region for each transect. On average, this This area eovered acorresponds to approximately 1 km longof glider transect, overtrack, along which about ten profiles were gathered.

280 typically obtained. The model captured the three-layered structure of the water column with the warm surface layer (upper mixed layer—UML), cold intermediate layer (CIL), and saltier deep layer. The depth ranges between the UML and the CIL were 7-22 and 6-24 m (I mission), 13-39 and 12-29 m (II mission), 10-43 and 6-41 m (III mission) for the measurements and the model, respectively. However, the model tended to overestimate the temperature in the CIL and underestimate salinity, particularly in the deep layer (Fig. 3a-c). On average, the modelled salinity was 0.4 g kg⁺lower than the measured salinity, and the CIL temperature was higher by about 2 and 1.5 °C than the measured temperature in 2018 and 2019, respectivelyprofiles were averaged over a 1×1 km area located within the same overlapping region.

Temporal developments of temperature and salinity distributions, stratification, and spice from the simulation and glider observations are shown in Figs. 3–6. A three-layered structure of the water column, consisting of a warm surface layer (upper mixed layer, UML), a cold intermediate layer (CIL), and a saltier deep layer, was observed and simulated. Observed patterns of variability in temperature and salinity distributions were well simulated by the model (Figs. 3–4). Despite—these discrepancies In absolute values, salinity was underestimated by 0.4 g kg⁻¹, while CIL temperatures were overestimated by approximately 2 °C in 2018 and 1.5 °C in 2019 in the model. In general, the model replicated the characteristic layered vertical

However, when characterizing the vertical structure and stratification of the water column, we point to some discrepancies. The observed and modelled UML depths were in close agreement during Missions I (7 ± 3.7 m and 7 ± 3.1 m) and II (13 ± 4.4 m and 13 ± 3.7 m) but diverged more in Mission III, with an observed average depth of 10 ± 4.4 m compared to 6 ± 2.6 m in the model. The depth of the CIL was reasonably well captured by the model in Missions I and III, with average observed and simulated depths of 22 ± 5.0 m and 24 ± 5.5 m, and 43 ± 5.2 m and 41 ± 6.0 m, respectively – both within the uncertainty of the estimates. However, a significant discrepancy was evident in Mission II, where the model placed the CIL approximately 10 m shallower than observed (29 \pm 5.1 m vs. 39 \pm 5.5 m). The observed and simulated depths of the maximum N² were, respectively, 10 ± 5.9 m and 8 ± 4.0 m during Mission I, $20 \pm$ 7.5 m and 15 m ± 4.1 m during Mission II and 14 ± 4.8 m and 9 ± 3.2 m during Mission III. These differences in the strength, structure and location of, ranging from approximately 2 to 5 m, indicate a systematic underestimation of the depth of the strongest stratification in the upper water column by the model. Partly, this could be related to an overall weaker salinity gradient in the model compared to observations. For instance, in the first half of Mission II (spring 2019), the strongest vertical density gradient, as indicated by the maximum N2, was determined by the vertical salinity distribution, as indicated by the glider data, whereas the model placed it shallower where the seasonal thermocline can be indicated. The maximum vertical density gradient was at depths about 10 and 8 m (I mission), 20 and 15 m (II mission), and 14 and 9 m (III mission) based on the measurements and the model (Fig. 3). Thus, the model positioned the upper pycnocline at shallower depths than measured began to develop. Furthermore, the model did not capture the presence of two occasionally observed two local maxima of vertical density gradient in the upper part of the water column in N2, e.g., on 21-30 May 2018 and 23-28 July 2019 (Fig. 4)-5). On both occasions, glider observations revealed two distinct stratification peaks: respectively, at 7 ± 2.7 m with the maximum N^2 of $0.0026 \pm 0.0005 \text{ s}^{-2}$ and at $19 \pm 4.2 \text{ m}$ with $0.0016 \pm 0.0003 \text{ s}^{-2}$, and at $6 \pm 2.8 \text{ m}$ with $0.0023 \pm 0.0007 \text{ s}^{-2}$ and at 19 ± 2.5 m with 0.0023 ± 0.0003 s⁻². The model showed a single stratification maximum of approximately 0.0017 ± 0.0003 315 s^{-2} at 6 ± 2.6 m on 21–30 May 2018 and 0.0041 ± 0.0008 s^{-2} at 5 ± 1.0 m on 23–28 July 2019. These discrepancies suggest that the model underrepresents the vertical complexity of stratification in the upper water column, the point that will be discussed in the Discussion section. The halocline was generally less pronouncedweaker in the model than in the observational data during all glider missions (Figs. Fig. 5). However, as our 3-4). Since we focus is on the seasonal thermocline (upper pycnocline UP), we do not analyse this discrepancy herefurther and assume that it does not its impact the following results regarding the structure and on the upper-layer variability in the UP is minimal. Vertical distributions of spice were similar in According to both the measurements and the simulation, although the maximum spice intensities were slightly lower in the model than in observations during both spring missions (Fig. 3d f). The spice variabilityspice intensity was the highest during the summer 2019 mission when (Fig. 6a-c), coinciding with the period of strongest vertical gradients in temperature, salinity, and density gradients were the largest, and the vertical most intense

density structure of the water column in the GoF and the development of the seasonal thermocline (Fig. 4), Only some slight5).

295

305

310

325

patterns of spice—was, were generally consistent between the highestmodel and observations; however, the model tended to underestimate the maximum spice intensities during spring missions. Nevertheless, both datasets point to a potential relationship between the development of stratification and SMS variability (processes). During the spring missions (May–June 2018 and 2019), spice maxima were located around the base of the UML—and—. They occurred at shallower depths (corresponding to lower densities) than the depth (density) of the maximum vertical density gradient (UP depth). However, in July. In contrast, during the summer mission (July—August 2019₇), the spice peak was movedshifted to the greater depths, situated beneath the UML and was located-immediately below the UP (strongest density gradient).

330

350

To identify whether the changes in the distribution of spice revealed for the glider missions are characteristic of seasonal development, To extend this analysis, we present monthly average spice-stratification parameters and vertical distributions derived of spice from the model data inoutput for May—through August 2018 and 2019 were analysed. As seen in (Fig. 5, the 6d-g). The density range between the UML and the CIL depths-increased from Mayspring to August. Likelate summer, indicating a deepening and strengthening of the pycnocline. Both the UML depth, and the depth of the maximum density gradient moved to the shifted toward lower densities from spring to late summerover the season, except betweenin July and—August 2018.

when this trend was less pronounced. In May of both years, the maximum spice intensity was at lower densities than those corresponding to the UML depth and the depth of the maximum density gradient. In From June—to August, the maximum spice intensity was identified aroundmaxima aligned more closely with the density corresponding to the depth of the maximum vertical density gradient. High, suggesting a seasonal deepening of spice variability. Elevated spice intensities were characteristic for a relatively broadspread over a broader density range, which increased from June to August, as also the pycnocline covered a larger density range in July—August than in June. The spice maxima were mostly immediately below the maximum density gradient (except June and July 2019). Furthermore, in June 2018 and August 2019, another local maximum of spice intensity was detected closer to the sea surface (at low densities), over the summer months, reflecting the seasonal development of the pycnocline.

Further, in June 2018 and August 2019, a secondary local maximum of spice intensity was detected closer to the sea surface at low densities, indicating enhanced variability in the upper layer during these periods. This suggests that while the primary spice variability deepens with the season, episodic events can still induce significant variability in the upper layers.

Comparing the two years, 2019 exhibited a more pronounced seasonal progression in spice distribution, with a clearer deepening and broadening of the spice-rich layer from May to August. In contrast, 2018 showed a less consistent pattern, particularly in July–August, when the expected shift toward lower densities was not as evident. These interannual differences highlight the influence of varying atmospheric and oceanographic conditions on the seasonal development of spice variability.

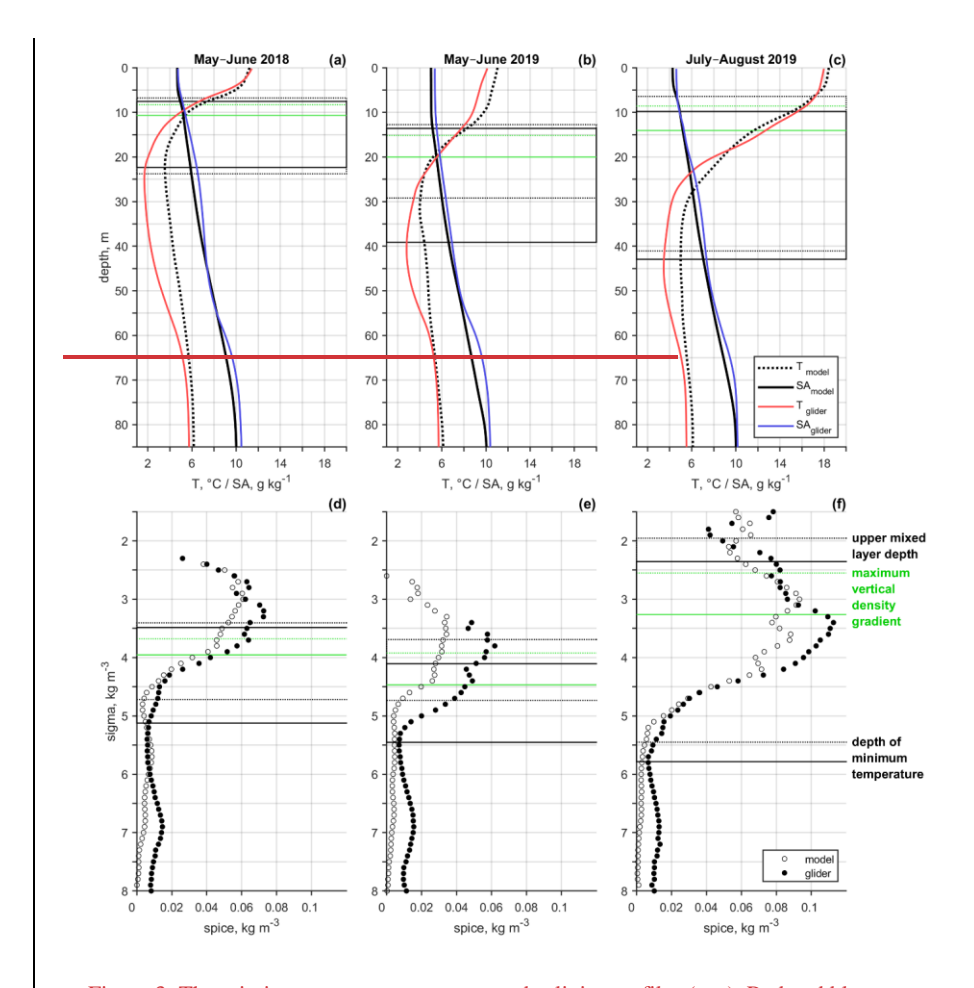


Figure 3: The mission average temperature and salinity profiles (a-c). Red and blue correspond to

temperature and salinity from the observations and dashed and solid black to temperature and salinity
from the model simulations. The standard deviation of spice calculated from the measurements (black
dots) and the modelled data (white circles) in each mission are shown on panels d-f. Columns I-III
stand for May June 2018, May June 2019, and July August 2019. The black horizontal lines (solid,
measurements; dashed, model) highlight the average upper mixed layer depth and the depth of
minimum temperature. The green horizontal lines highlight the average position of the maximum

vertical density gradient. The glider data were averaged in the chosen area (Fig. 1), and the model data in a 1×1 km window (Fig. 1).

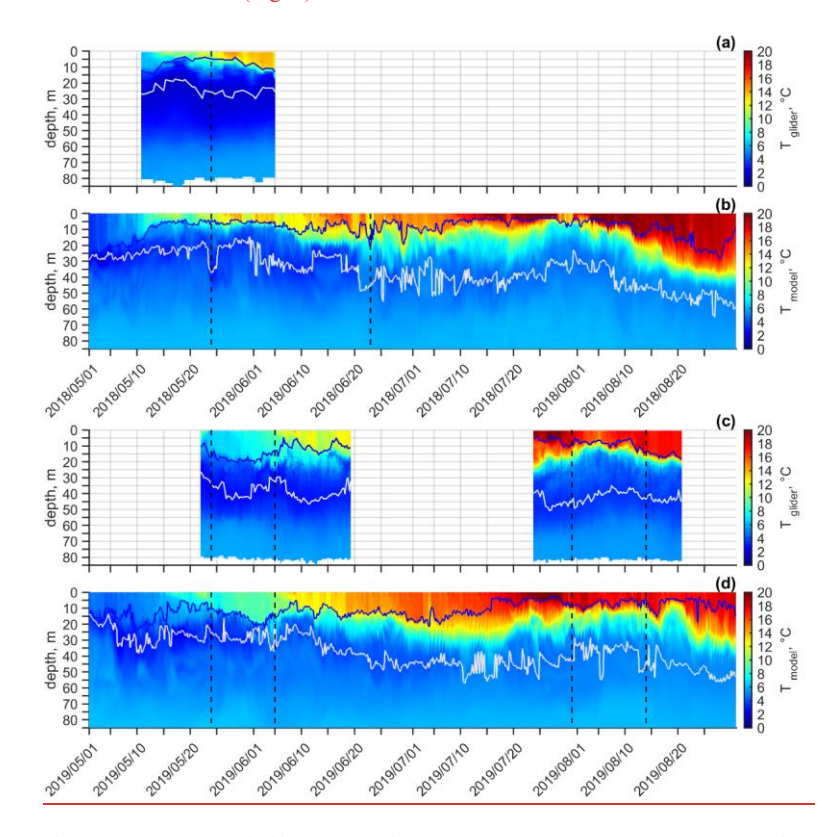
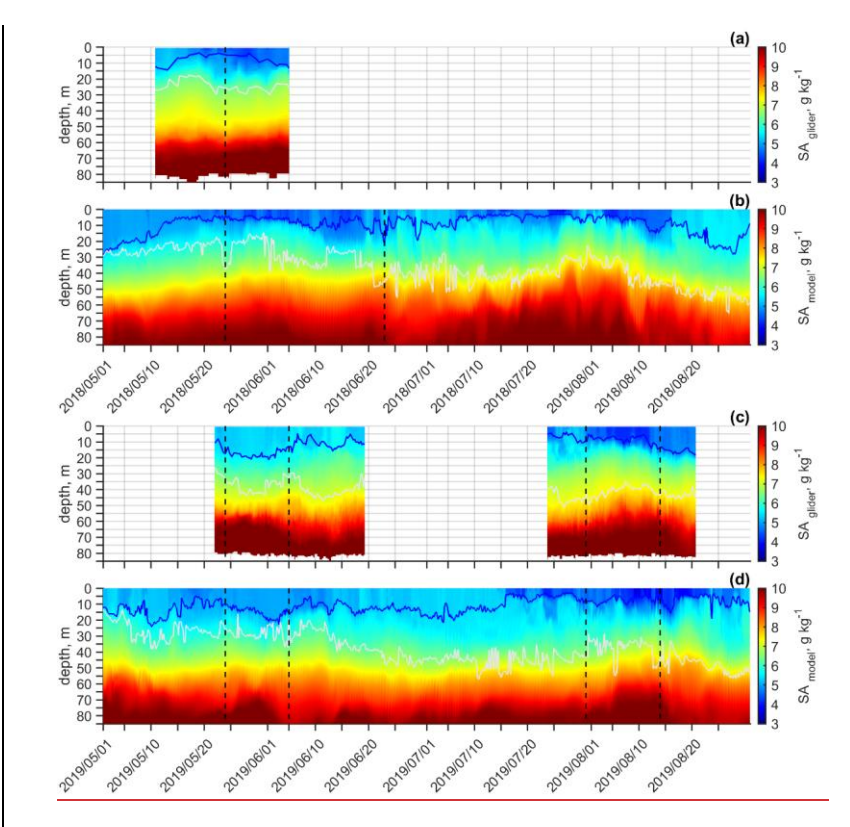
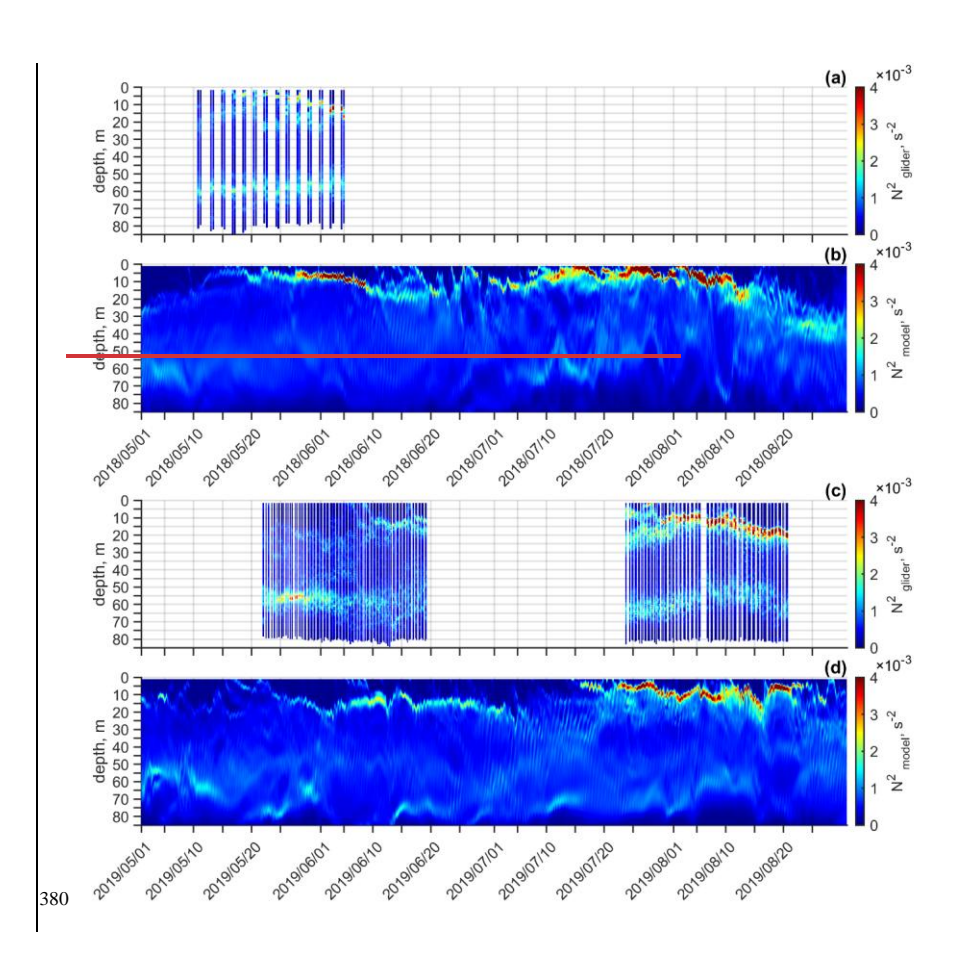


Figure 3: Temperature variability based on glider data (panels a, c) and model data (panels b, d) for May–August 2018 (a, b) and 2019 (c, d). The glider data represent average profiles for each section within the selected area, forming a composite temperature field. The model data show average profiles within a 1×1 km window at each model output time. Blue and white lines indicate the depths of the UML and the CIL, respectively. Vertical black lines indicate the dates shown in Figure 8: 24 May 2018 and 23 June 2018 (panel a, b); 24 May, 5 June, 31 July, and 14 August 2019 (panel c, d).



375 Figure 4: Salinity variability based on glider data (panels a, c) and model data (panels b, d) for May-August 2018 (a, b) and 2019 (c, d). The glider data represent average profiles for each section within the selected area, forming a composite salinity field. The model data show average profiles within a 1×1 km window at each model output time. Blue and white lines indicate the depths of the UML and the CIL, respectively. Vertical black lines indicate the dates shown in Figure 8: 24 May 2018 and 23 June 2018 (panel a, b); 24 May, 5 June, 31 July, and 14 August 2019 (panel c, d).



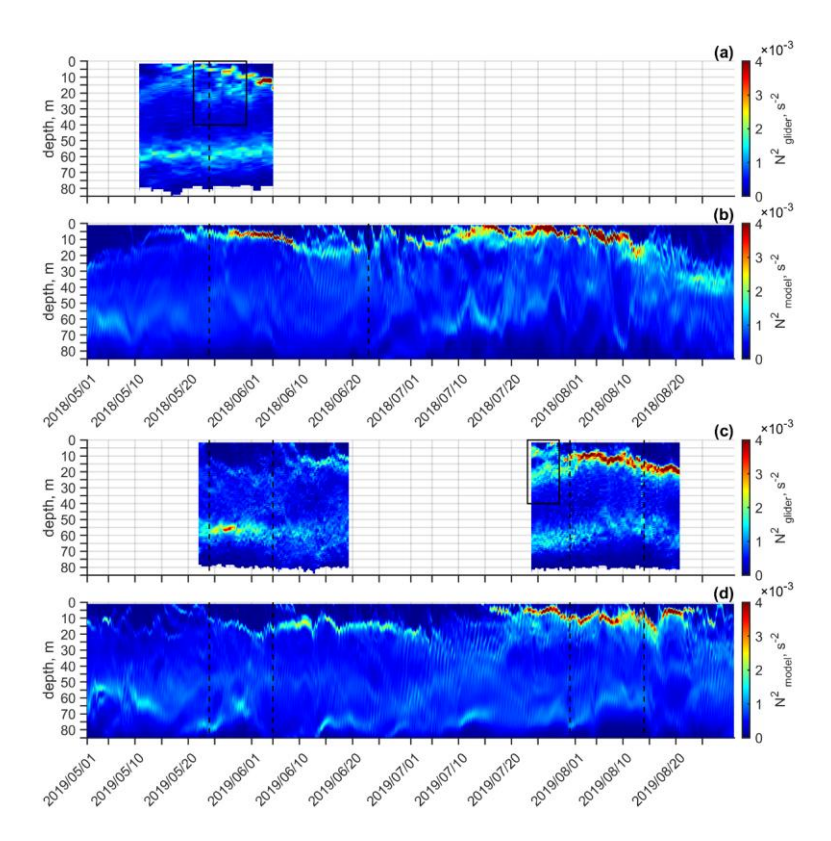


Figure 4: Dynamics 5: Variability of vertical stratification presented as Brunt-Väisälä frequency squared (N^2) based on glider data (panels a, c) and model data (panels b, d) infor May-August 2018 (a, b) and 2019 (c, d). The glider data show therepresent average profile perprofiles for each section inwithin the ebosenselected area (Fig. 1), and the, forming a composite salinity field. The model data anshow average profile inprofiles within a 1×1 km l km window (Fig. 1at each model output time. Vertical black lines indicate the dates shown in Figure 8: 24 May 2018 and 23 June 2018 (panel a, b); 24 May, 5 June, 31 July, and 14 August 2019 (panel c, d). Black boxes indicate periods of two observed local maxima in N²: 21–30 May 2018 (panel a) and 23–28 July 2019 (panel c)

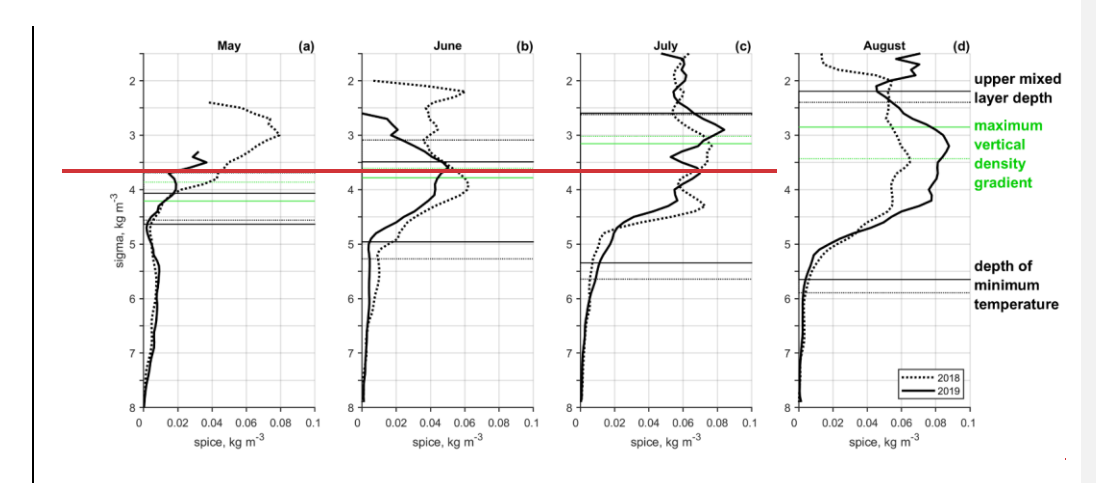


Figure 5. Monthly standard deviation of spice from May to August in 2018 (dashed) and 2019 (solid). Panels a-d stand for different months. The black horizontal lines highlight the average upper mixed layer depth and the depth of minimum temperature. The green horizontal lines highlight the average position of maximum Brunt-Väisälä frequency (vertical density gradient) referred to as the upper pyenocline (UP). The model data were averaged in a 1×1 km window (Fig. 1).

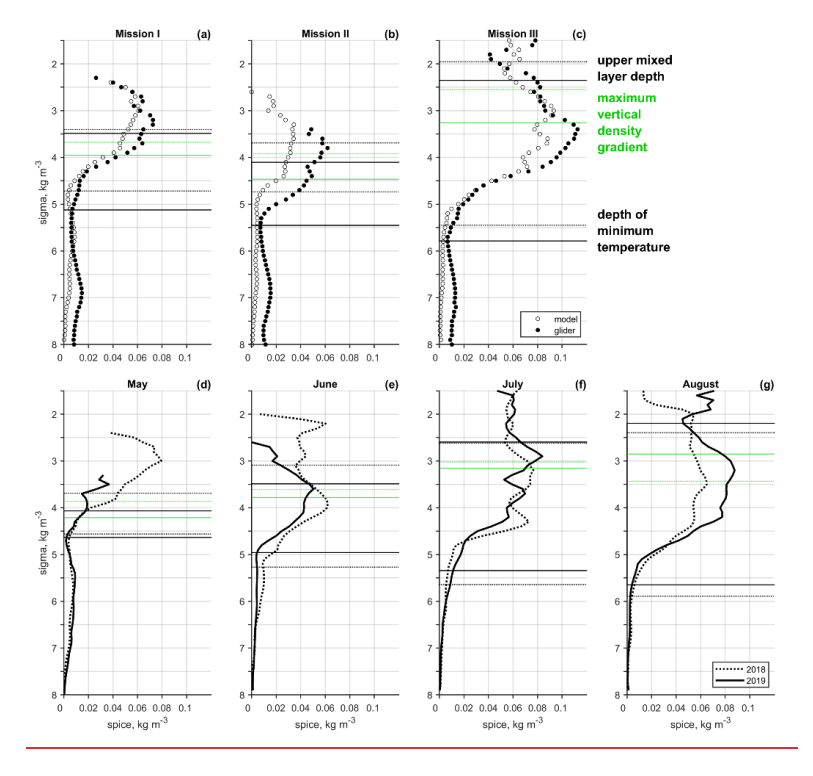


Figure 6: The standard deviation of spice. (a–c) First row: measured (black dots) and modelled (white circles) spice variability for each glider mission period. Solid and dashed black lines mark the average UML depth and depth of minimum temperature from measurements and model, respectively. Green lines indicate the average depth of maximum Brunt-Väisälä frequency. (d–g) Second row: monthly standard deviation of modelled spice from May to August in 2018 (dashed) and 2019 (solid). Black and green horizontal lines represent the same reference depths as in panels a–c. All dashed lines correspond to 2018, and all solid lines to 2019. Model data were averaged over a 1×1 km area (see Fig. 1).

3.2 Background forcing and large-scale and mesoscale dynamics

395

400

Background forcing in the study area in May–August 2018 and 2019 was characterized by mostly positive net surface heat flux (Q) and variable wind conditions (Fig. 6). There were 7). Short periods withof negative Q at the beginning of occurred in early June and July 2018-and in, August 2018, as well as at the beginning of early May and July 2019, and again in late July andto early August 2019. Note that easterly Easterly and north-easterly winds-could generate, which favour upwelling events

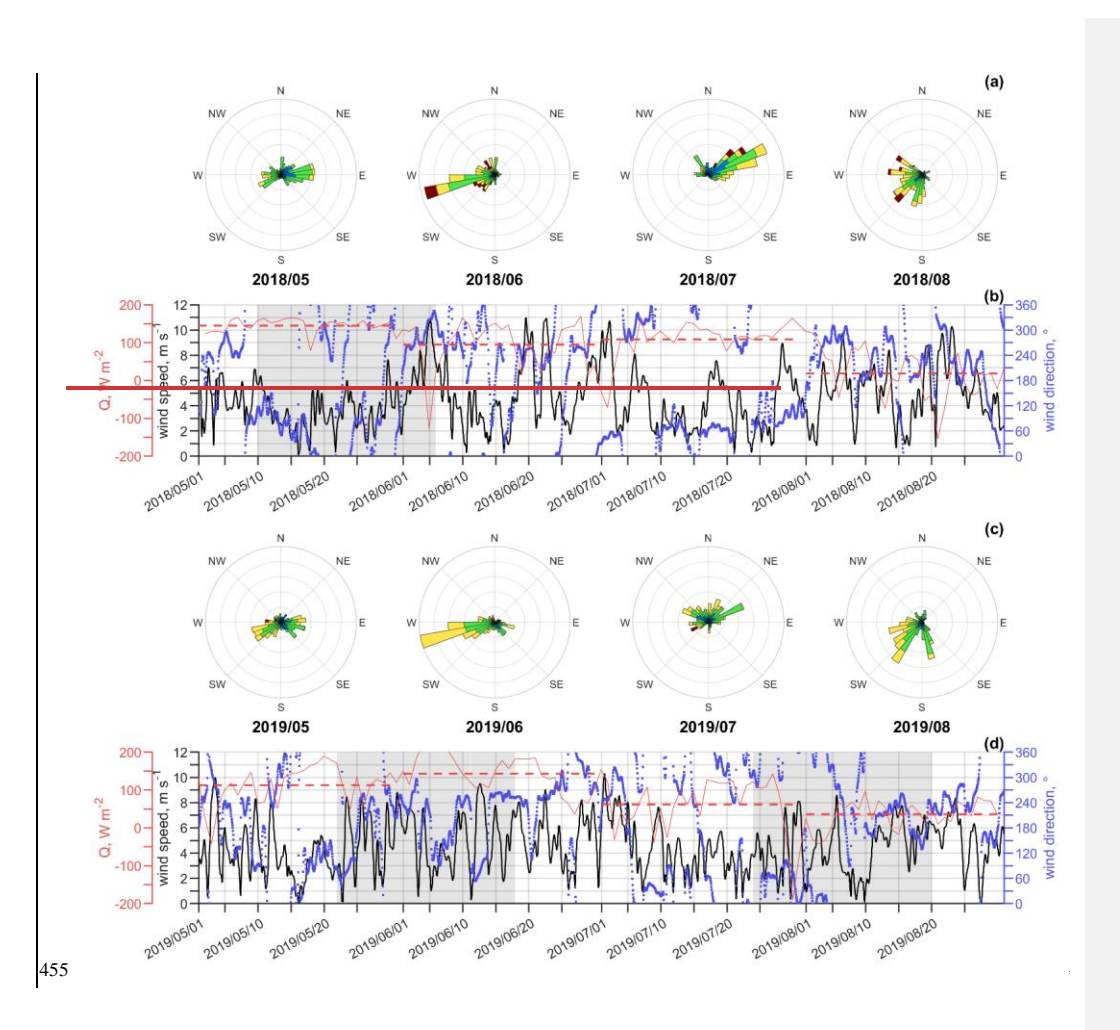
roses suggest that upwelling favourable winds dominated in the study areawere prevalent in July 2018 and were well represented also notable in May 2018 and May and July 2019 (Fig. 6a7a, c). Downwelling Conversely, downwelling-favourable westerly and south-westerly winds dominated in June of both years. Southerly winds August wind patterns were marked by frequent in August of both years, and southerly winds, while northerly winds occurred frequently were more common in July 2019. Wind speed rarely exceeded 10 m s⁻¹, except in June 2018, when three periods withepisodes of strong westerly winds were observed occurred. These winds leading events led to vertical mixing and downwelling in the study area caused a, resulting in deepening of the thermocline and weakening of weakened upper layer stratification. N² peaked in the upper layer inearly June 2018, decreasing from 0.006 s⁻² on 2 June to 0.002 s⁻² by 10 June, accompanied by a deepening of its maximum from 5 m to 15 m (Fig. 4b5b). Similarly, downwelling—favourable winds and negative Q at the beginning of July 2019 resulted in the weakening of contributed to reduced vertical stratification. The already weak stratification, characterized by a maximum N2 of 0.002 s⁻² at 18 m depth, weakened further between 1 and 5 July, with the depth of the maximum shifting to 30 m (Fig. 4d). There were several weekly or bi-weekly periods with 5d). Several calm weatherperiods lasting about one to two weeks, namely in May and July of both years allowing, allowed for the development and strengthening of vertical stratification. Substantial stratification strengthening occurred in May and July 2018, with N2 maxima peaking at 0.006 s⁻² and 0.01 s⁻², respectively (Fig. 5b). In contrast, by the end of July 2019, the N² maximum reached only 0.005 s⁻² (Fig. 5d). In August, SW-W winds dominated in both years, and Q was no longer predominantly positive. We suggest that wind forcing and surface heat flux played a crucial role in shaping the thermohaline variability in the area, which differed with notable differences between the two years. To describe better illustrate how atmospheric forcing influenced the development of background hydrographic conditions in relation to atmospheric forcing in more detail, we present somea series of characteristic situationsevents from spring-summer 2018–2019. In May 2018, NE-E winds (Fig. 667b) triggered upwellings along the southern coast, evident in narrow coastal regions with low temperatures (Fig. 7a). A-8a). Concurrently, a broader westward flow along the southern coast transported warmer, less salty surface water from the easteastern GoF into the study area (Fig. 7a, d, g8a). In June 2018, strong SW-W winds led to downwelling along the southern coast (Fig. 7i, m, p). 8b), deepening the thermocline and altering the upper-layer structure. In May 2019, upwelling along the southern coast was more intense than in May 2018 (Fig. 7b, e, h), the previous year, driven by a strong E wind impulse on May 22–23 (Fig. 6d). 7d), resulting in pronounced cold water intrusions along the southern coast (Fig. 8c). By June 2019, upwelling subsided as SW-W winds dominated, creating became dominant, leading to the formation of mesoscale rotating structures in the gulf's centre central gulf (Fig. 7k, n, q8d). In late July 2019, NE-E winds during the last fiveover several days of the month (Fig. 6d)7d) once again caused upwelling along the southern coast (Fig. 7c, f). A. accompanied by a strong surface-layer outflow from the gulf developed in the surface layer (Fig. 7i8e). This outflow weakened

nearalong the southern coast of the GoF, while westerly and south-westerly could lead to downwelling events. Monthly wind

in early August as northerly winds and negative Q prevailed and average negative heat fluxes were observed (Fig. 6d7d).

440 differentdistinct water masses (Fig. 71, o, r8f). ThusOverall, the dynamical background varied substantially duringacross the study period, reflecting a strong influence of episodic atmospheric forcing. Depending on the prevailing wind forcing, conditions, mesoscale features such as upwellings of varying intensity and associated westward currents (see flows (Fig. 7a i8a, c, e), downwellings (Fig. 7j, m, p8b), and eddies (Fig. 7k, n, q and 7l, o, r) developed 8d, f) developed. These features coincided with enhanced SMS activity, as evidenced by 445 elevated Ro and intensified horizontal buoyancy gradients in the surface layer, particularly near frontal zones and filaments. In May 2018, May 2019, and July 2019 (Fig. 8a, c, e), strong lateral gradients and Ro O(1) emerged near the southern coast, aligning with coastal upwelling. Further, the westward intrusion of low-salinity water from the eastern part of the gulf played a notable role in maintaining lateral density gradients across the basin, particularly in August 2019 (Fig. 8f). The SMS-active regions were more pronounced in summer (Fig. 8b, e, f), likely due to sharper lateral density gradients and a shallower mixed layer, that reduced the local Rossby deformation radius and favoured stronger SMS instabilities by intensifying frontal sharpness and enabling ageostrophic motions at the mesoscale. smaller scales. Transient wind events and air-sea fluxes emerge as key drivers of mesoscale and SMS variability in relation to these features on the background of the GoF, generating conditions that favour the development of vertical stratification is analysedSMS instabilities. The resulting SMS activity and its spatial distribution are examined in the following subsectionsection.

However, a westward flowadvection of fresher water persisted, making the study area a transition zone between



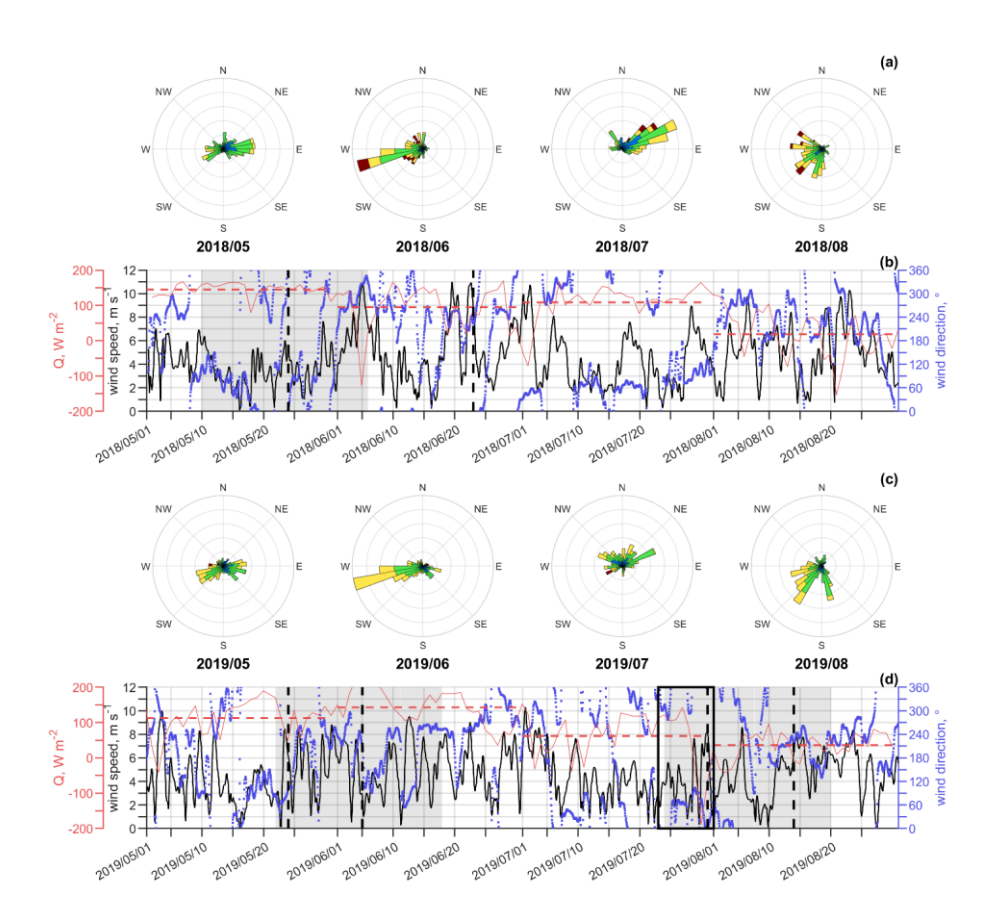
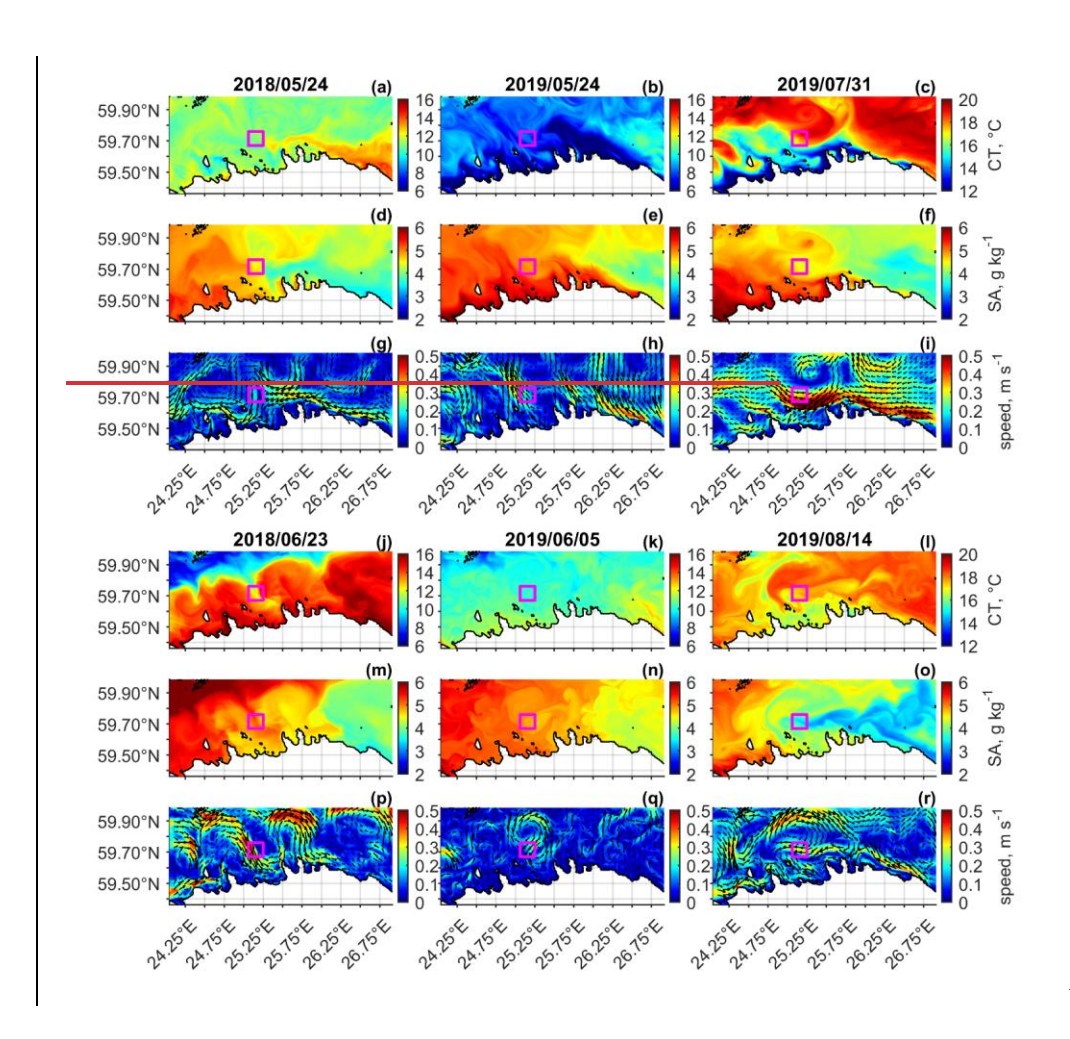


Figure 6.7: The daily average net surface heat flux, Q, (red, dashed line showing the monthly average), wind speed (black) and direction (blue) in spring-summer 2018–2019 (Panels b and d). Panels a and c show the wind roses from May to August for both years, respectively. Vertical black lines indicate the dates shown in Figure 8: 24 May 2018 and 23 June 2018 (panel b); 24 May, 5 June, 31 July, and 14 August 2019 (panel d). The black box indicates the period examined in subsection 3.4: 23–31 July 2019 (paned d).



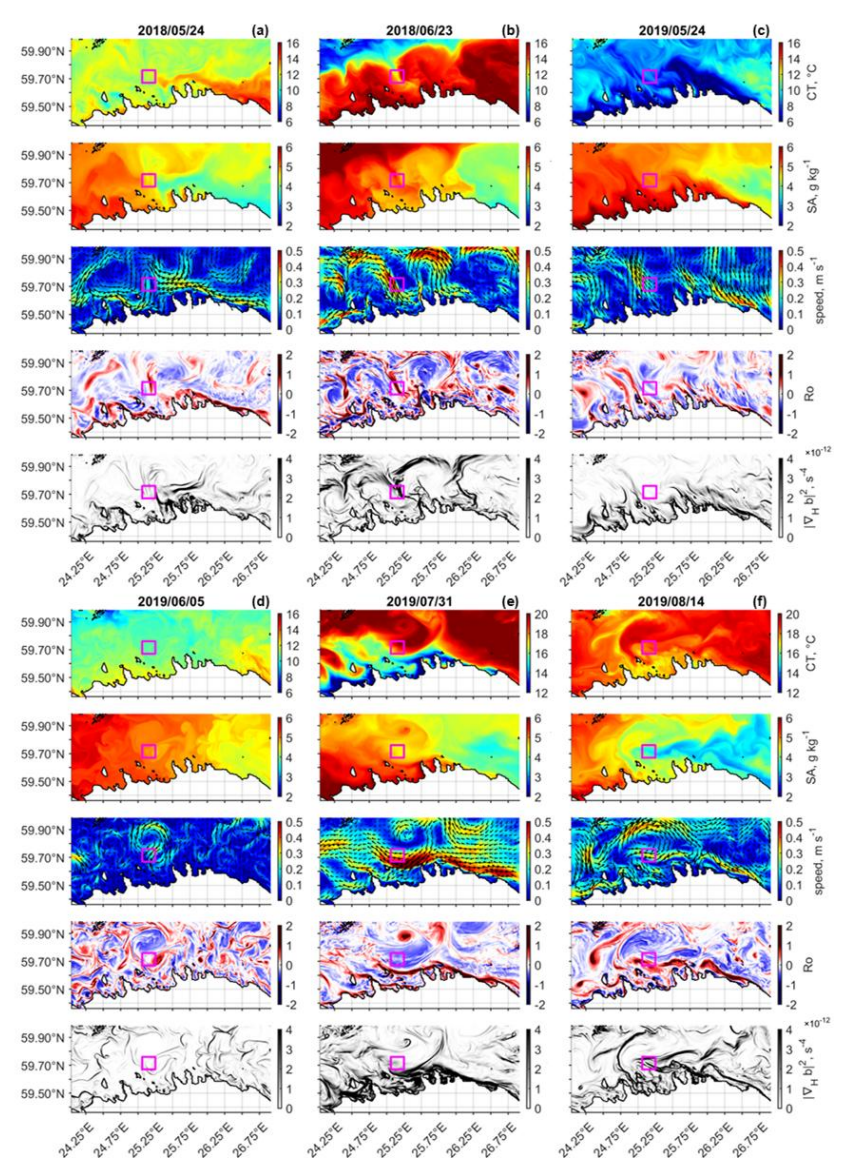


Figure 7. Thermohaline variability 8: Overview of surface hydrographic and dynamical conditions in the Gulf of Finland induring spring-summer 2018-2019. Panels show, illustrating the surface (0-3 m) temperature (a-c and j-l), salinity (d-f and m-o), and velocity distributions (g-i and p-r). Presented variability of SMS-relevant fields. Example dates in-characterizing the evolving dynamical background are shown in (a-c) first column-aerow: 24.05, May 2018 (a, d, g) and _23.06, June 2018 (j, m, p), and 24
May 2019, and in the (d-f) second column 24.05.2019 (b, e, h) and 05.06, row: 5 June 2019 (k, n, q), and in the third column_31.07, July 2019 (e, f, +i), and 14.08, August 2019 (l, o, r), For each date, panels from top to bottom display surface (0-3 m) Conservative Temperature (°C), Absolute Salinity (kg kg-i), velocity (m s-l), Rossby number, and squared horizontal buoyancy gradient modulus (s-l). The magenta box indicatesmarks the 10×10 km 10 km study window.

3.3 Submesoscale variability from spice in observations and model Submesoscale variability, instabilities and subduction

The intensity of submesoscaleSMS variability-characterized, quantified by the root mean square of spice-peaked on several occasions, which partly could be related to concurrent. displayed multiple peaks throughout the spring-summer periods of 2018 and 2019. Some of these peaks coincided with elevated surface Ro variability (indicated by local maxima of relative vorticity but oftenin the root mean square Ro; Fig. 9), such as during 25–27 July and early August 2018 or in August 2019, while others occurred in periods of under relatively low Ro conditions. Notably, high spice values (Fig. 8). For instance, in 2018, temporal maxima in spice intensity occurred simultaneously with Ro maxima on 25–27 July and at the beginning of August, right after a temporal Ro maximum on 15–16 August and during periods of low Ro-were observed on 18 June and 11–13 July (Fig. 8b). Similarly, in 2019, temporal spice maxima coincided with Ro maxima in August, while the largest spice intensity values on 22–30 July were revealed on the background of relatively low Ro values (Fig. 2018, as well as between 22 and 30 July 2019, despite moderate to weak Ro variability (Fig. 9b, d). This partial decoupling suggests that spice may capture a broader spectrum of SMS variability, including processes less directly linked to elevated relative vorticity. 8d).

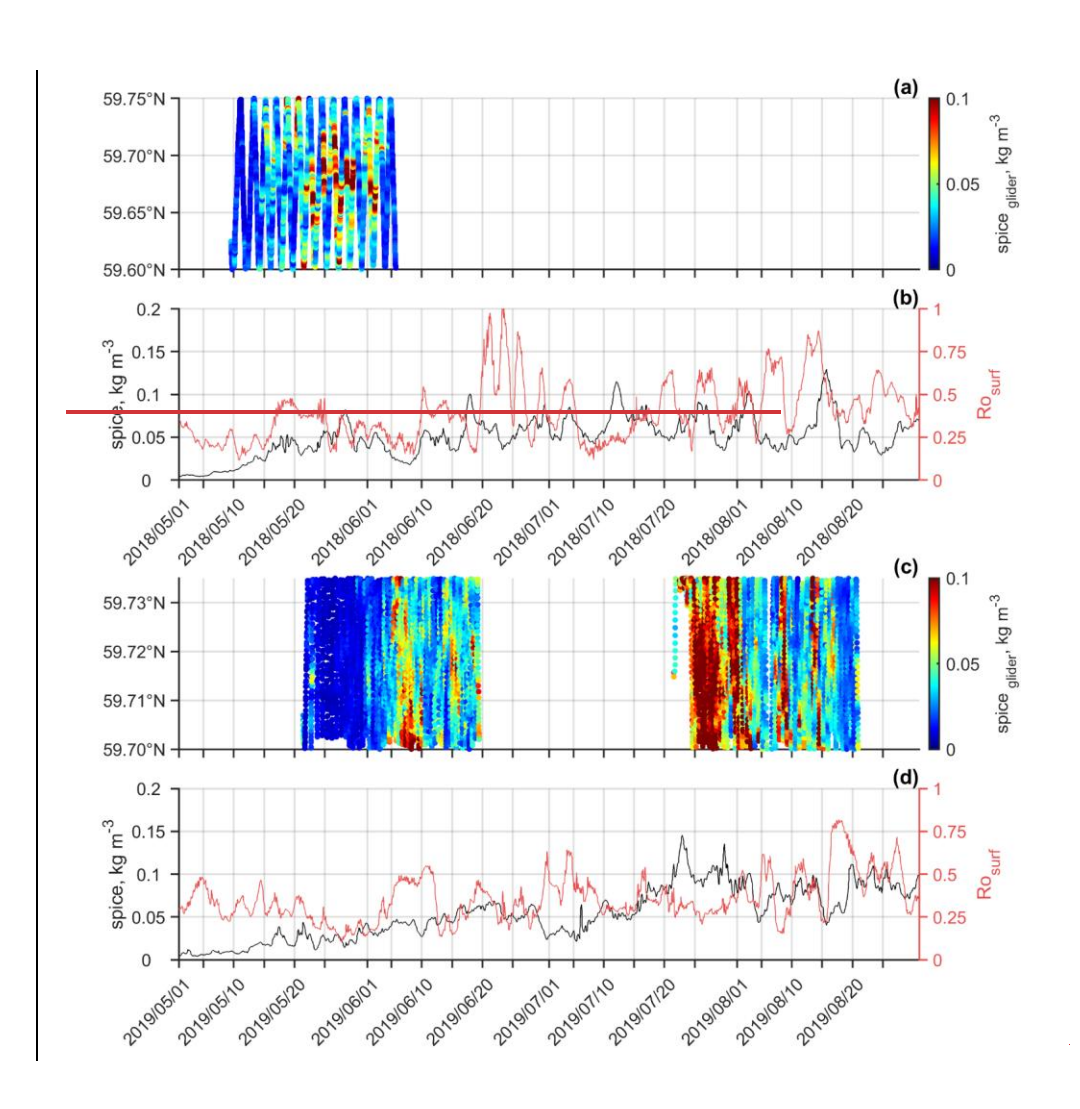
Note that spiceSpice intensities calculated from glider data and model data agree qualitatively wellshow good qualitative agreement, considering that for the latter, data frommodel values were averaged over the defined time series box were used (see the box in Fig. 1 and; compare Figs. 8a9a and 8b9b, and Figs. 8e9c and 8d). Furthermore, on average, the9d). Both datasets reveal an overall increase in spice intensity increases from May to August—due to, reflecting the development of seasonal strengthening of stratification (which is at its maximum in July—August) and enhancementthe intensification of background gradients of both temperature and salinity. Relative vorticity also undergoes an average increasing trend from May to August, although some—gradients. This seasonal trend is further supported by a concurrent rise in Ro, punctuated by transient peaks driven by episodic strong wind forcing events (, as in late June 2018) could create temporal high peaks in Ro (Fig. 8b9b). We picked upselected three occasionsperiods when both glider and model data were available to demonstrate the relationship

490

495

between how the distribution patterns of parameters indicative of the development of submesoscale SMS instabilities/processes and relates to spice. The intensification of spice observed in the second half of May 2018 observed by glider measurements (Fig. 8a9a) and simulated by the model (Fig. 8b9b) coincided with the eastward transport of warmer, less saline water and the formation of horizontal buoyancy gradients (Fig. 8a). During 15–25 May, calm weather prevailed, and transport of less saline and warmer waters from the eastRo, (Fig. 7j, m). First, an increase in Ro (averaged over the time series box), exhibited a sustained increase towards O(1) occurred, and then), indicating enhanced SMS activity in the surface layer. The spice intensity

peaked concurrently increased, with notable peaks on 18 and 25 May, and reached its maximum on 28 May (Fig. 8b), Figure 9a, d9b). Figures 8a and g10d demonstrate the presence of elongated SMS structures withon 24 May, characterized by Ro O(1) Ro.), Ri <<1, and relatively strong horizontal buoyancy gradients on 24 May. Elevated spice intensity was detected located near these features, indicating enhanced thermohaline variability associated with SMS instabilities. (Fig. elongated structures (Fig. 9i).10d). In late May 2019, an intense upwelling occurred along the southern coast (see an example one.g., 24 May in; Fig. 7b, e), but no significant 8c). However, this did not lead to a notable increase in the spice intensity and or Ro was observed (Fig. 8d) in within the time series box- (Fig. 9d). A considerable rise in Ro and slightly the modest rise in spice intensity increased occurred at the beginning of June, coinciding with the changing wind forcing (Fig. 6d). A a change from SW winds on 1 June to SE winds on 5 June (Fig. 7d). During this period, a cyclonic eddy ((~10 km in diameter—10 km) formed in the study area, 510 accompanied by a larger anticyclonic eddy in the offshore area (Fig. 8d). 9b). Order one Elevated Ro from 5 to 11 June indicated the persistence of this cyclonic feature in the time series box (Fig. 8d). Figure 9b, e, h and k illustrate elevated 9d). Elevated spice intensity was observed at the periphery of the cyclonic eddy eoinciding(Fig. 10e), aligned with narrow stripes of relatively high buoyancy gradients and low Ri- (Fig. 8d and 10b). The highHigh spice intensity inobserved during the third trimesterweek of July 2019 (Fig. 8e9c, d) may be linked appeared to 515 thebe associated with varying wind forcing (Fig. 7d) and the development of a westward current along the southern coast of the GoF (Fig. 748e). Westerly winds at the beginning of July were followed by upwelling—favourable winds on 7–10 July, which evoked the westward coastal current. After that, a period of weaker variable winds occurredfollowed, and a newthen another stronger pulse of easterly winds intensified this occurred, further strengthening the coastal current. However, a relatively low Despite the dynamic conditions, Ro was detected on the surface in within the time series box remained relatively 520 low during this period (Fig. 8d). Nevertheless, as seen in Fig. 9c and f, a region 9d). However, Figure 8e reveals that regions of high-Ro O(1) and strong horizontal buoyancy gradients linked to the intense-coastal current were located to the just south of the study area. Interestingly, patches of low Ri wereappeared also revealed to the north from of the region of with the highest surface current speeds and patches, while areas of high spice intensity were revealed found even further to the farther north (Fig. 9i and 1). Since also later, episodic increases in the 10c, f). The observed spatial offsets between Ro, Ri, and spice intensity in the subsurface layer (for instance, observed on 8-9 and 13-14 August 2019, Fig. 8c) did not correlate with the peaks in the Ro atsuggest that active SMS processes may be vertically and/or laterally displaced from the surface, we analyse this situation in more detail frontal zone. These patterns motivate a closer inspection of the late July period.



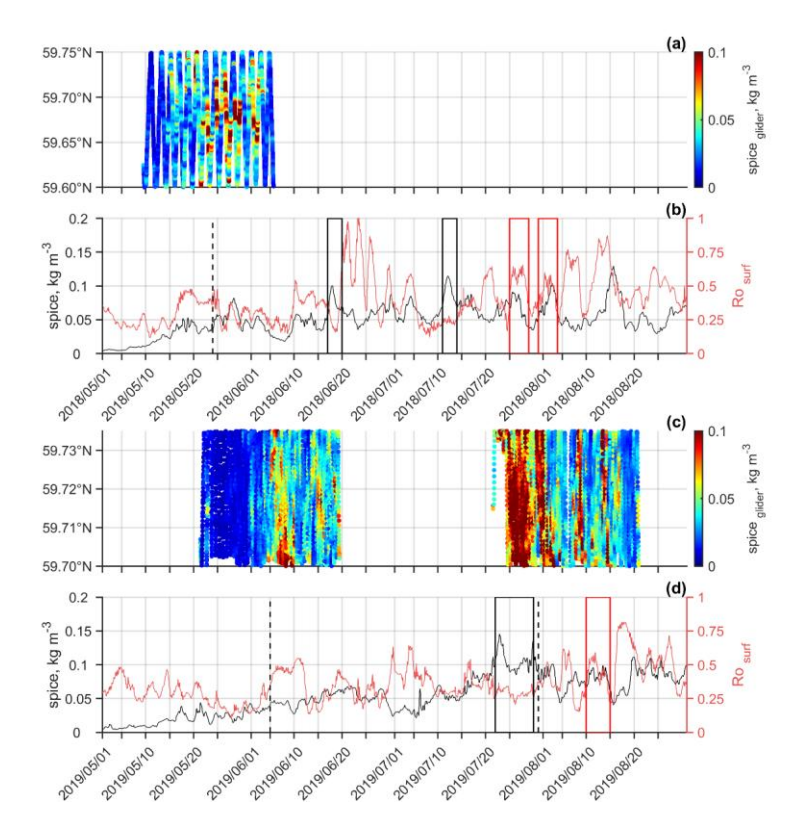
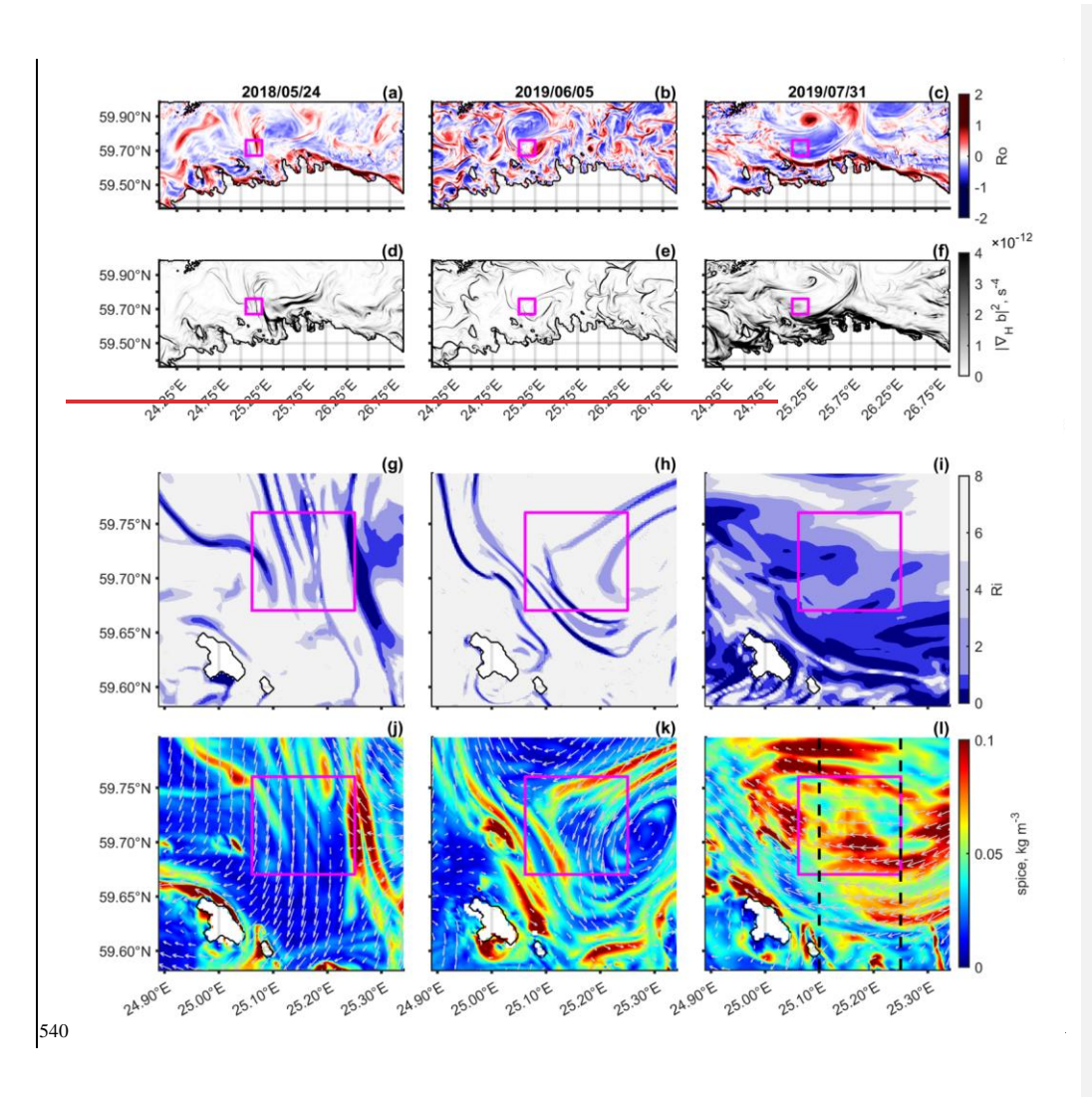


Figure 8. The root mean square spice in the density range limited from the surface to the depth of minimum temperature in spring-summer 2018–2019. Panels a and c show the intensity of spice along the glider trajectory. Panels b and d show the results from the model, which were calculated in a 10×10 km study window. Black line shows the spice and red line the root mean square Rossby number on the surface.

Figure 9: Root mean square spice in the density range from the surface to the depth of minimum temperature in spring-summer 2018–2019. Panels a and c show spice intensity along the glider trajectory; panels b and d show model results, calculated within a 10×10 km study window. The black line shows spice, and the red line indicates the surface root mean square Rossby number (Ro). Vertical black lines mark the dates shown in Figure 10, corresponding to periods discussed in subsection 3.3: 24 May 2018 (panel b), and 5 June and 31 July 2019 (panel d). Red boxes highlight example periods of high spice and high Ro, while black boxes indicate periods of high spice and low Ro (panels b and d).



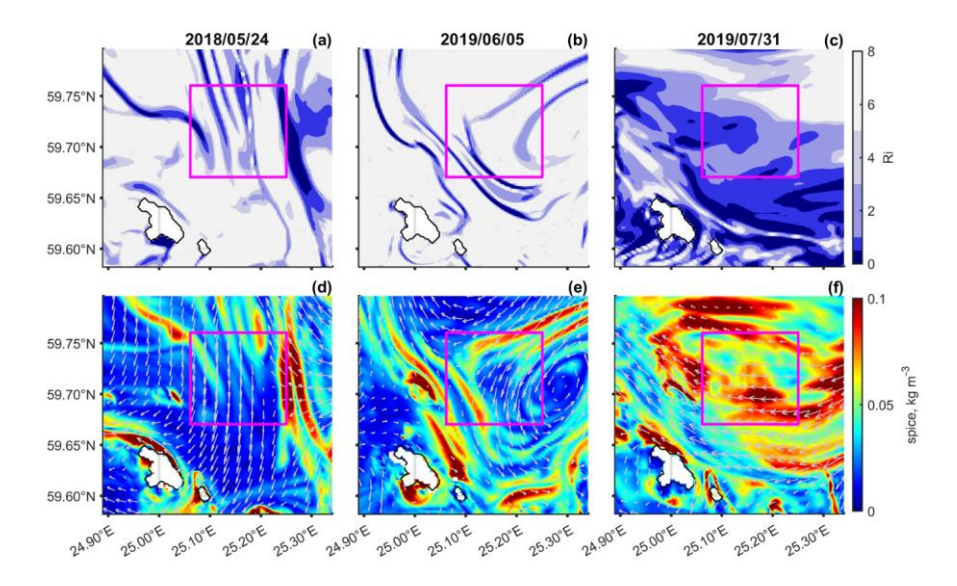


Figure 9. The quantities indicative of the SMS regime on the sea surface and the intensity of spice in the density range limited by the depth of minimum temperature in spring summer 2018, 2019. An example date is shown from each glider mission period (I–III stand for May June 2018, May June 2019, and July August 2019, respectively). Panels show Rossby number (a-c), squared horizontal buoyancy gradient modulus (d-f), Richardson number (h-i), and spice intensity (overlapped with surface currents) distributions (j-l), respectively. The magenta box indicates the 10×10 km study window, and the black lines in panel I marks the transects shown in Fig. 10.

Figure 10: Richardson number (a–c) and root mean square spice calculated within the density layer from the surface to the depth of minimum temperature (d–f) during spring–summer 2018–2019. Each column shows one example date from a different glider mission period – 24 May 2018, 5 June 2019, and 31 July 2019 – corresponding to the dates shown in Figure 8. The magenta box marks the 10×10 km study window.

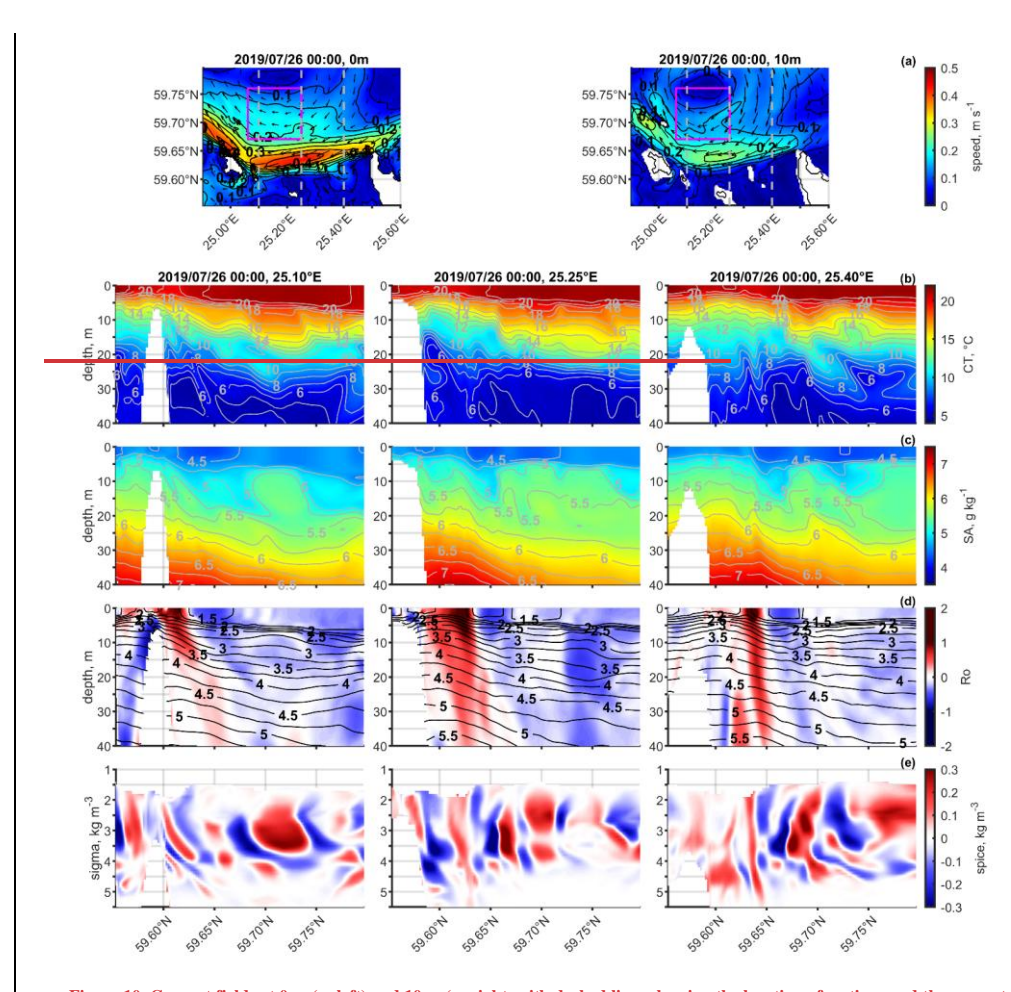


Figure 10. Current fields at 0 m (a; left) and 10 m (a; right, with dashed lines showing the location of sections and the magenta box the 10×10 km study window) depth on 26.07.2019. The colours indicate the speed, and the arrows indicate the direction of currents. Contours are shown with a step of 0.05 m s⁻¹. Vertical sections of temperature (b), salinity (c), Ro (d) and density anomaly, and spice (e) along meridians 25.10° E (left column), 25.25° E (middle column), and 25.40° E (right column) on 26.07.2019.

3.4 Upwelling-Driven Submesoscale Variability and Subduction

560

580

The distributions of currents, together with vertical sections of temperature, salinity, density, Ro and spice (Fig. 10), allow us to suggest the origin of intense submesoscale variability in the subsurface layer of the study area. Byperiod from 23 to 31 July 2019 was selected for closer analysis due to an observed peak in spice variability (Fig. 9d). For each day within this period, a set of vertical sections, as shown in Figure 11, was produced and is included in Supplement 1. Prior to the strong easterly wind impulse on 28–29 July, winds varied between NE and NW, averaging 3.5 m s⁻¹ (Fig. 7d). After 25 July, the easterly wind component strengthened, and by 26 July 2019, a strong coastal current had emerged (Fig. 10a), and accompanied by high subsurface variability in temperature and salinity was detected in the subsurface layer of the across all three selected sections (Fig. 10b, c). The highest Ro values in the area were associated with the Supplement 1). This current intensified by 29 July, coinciding with a clear upwelling event. Surface temperatures dropped from 22 °C, and northward velocities increased sharply in the upper layer (Fig. 11a–d). Isopycnals tilted, with an outcropping of the 3 kg m⁻³ isopycnal (Fig. 11f), reflecting enhanced horizontal buoyancy gradients and frontal sharpening – conditions favourable for SMS instabilities.

Ro reached O(1) near the coastal current zone and topographic features (Fig. 10d);11f) while Ro values were-remaining relatively low in the offshore area (see-left panel in Fig. 10d11f and Ro curve in Fig. 8d). The isopycnals, which were in the subsurface layer offshore, were close to the sea surface at the sites with high Ro. Along isopycnal spice was high in a much larger area (Fig. 10e) than the intense coastal current at all sections and in the time series box 9d). Vertical velocities increased notably across all transects (Fig. 8d). It suggests that the high SMS variability in the offshore area could originate from the mixing of converging water masses with different TS-characteristics likely due to the SMS instabilities of the observed current11e), and horizontal velocity fields indicated intensified shear in the upper 40 m (Fig. 11c, d). These dynamics are consistent with shear-driven instability and frontal subduction.

Distributions of surface currents and spice intensity in a larger area on By 29 July 2019, spice anomalies became more confined to the upper 15 m and showed weaker spatial alignment with elevated Ro (Fig. 11b, d; it characterizes the same situation as presented in Fig. 9, right column and Fig. 10) demonstrate a probable link between 11g), in contrast to 27–28 July, when enhanced subsurface spice was more closely aligned with regions of Ro O(1) (Supplement 1). Notably, spice extended beyond the core of the coastal current, with elevated values observed near sloping isopycnals and beneath frontal zones (Fig. 11g). These signals, aligned with tilted isopycnals, indicate both vertical and lateral thermohaline displacement.

Horizontal distributions of velocity and spice at the surface and 20 m depth (Fig. 12) highlight the influence of flow-topography, configuration of the coastline and interactions on SMS variability. The spice-At the surface, the coastal current veered offshore at several locations, particularly downstream of peninsulas and bathymetric irregularities (Fig. 12b). At 20 m, flow patterns differed significantly from the surface, especially near the coast where the flow reversed with depth, indicating strong vertical shear (Fig. 12b, d). Elevated spice intensity near these transitions (Fig. 12f) suggests that such flow structures contribute to the generation and modulation of SMS features. Spice intensity is thewas highest both along the coast and in offshore areas where the coastal current turns off the coastdeflected seaward, especially westward (downflow) from the of

at 25.50-25.75° E and low in the east. Smaller-scale irregularities in temperature and salinity distributions are evident at almost all topographic features reaching shallower than 40 m (Fig. 11f. h). Also, at longitudes 25.05 25.25° E (it corresponds approximately to the time series box), SMS variability at and below the thermocline and average spice intensity are relatively high (spice intensity was up to 0.2 kg m⁻³; Fig. 11j). 595 We compared the described patterns in the case of upwelling described above with those observed during downwelling development conditions in early July 2019. In On 3 July, the ease of downwelling, the surface current field was different from that described above, with characterized by prevailing shoreward transport and the presence of eddies in the surface layer (Fig. 11a). In contrast to the upwelling situation (Fig. 11d), spice intensity on 3 July 2019 was generally higher east of the larger peninsulas (Fig. 11c). The thermocline (upper pycnocline) was located deeper, and high SMS variability was associated with 600 all12a). The flow at 20 m roughly mirrored the surface (Fig. 12c), indicating weaker vertical shear, although localized shear zones were still present near topographic features (Fig. 11e, g, i). However, the average level of. High spice intensity between these topographic features was significantly present nearshore and, to a lesser extent, offshore (Fig. 12e), but overall spice intensity was lower in downwelling than inon 29 July. This contrast is further illustrated by zonal cross-sections (Fig. 13), which provide an alongshore view of the thermohaline and 605 dynamic structure during the two events. While the transects from 3 July and 29 July share some structural similarities, they also reveal key dynamic differences. Due to the alongshore orientation and its distance from the coast, signs of upwelling. It are more difficult to detect directly. However, meridional sections (Supplement 1) confirm the presence of upwelled water, indicated by surface temperatures below 20 °C and salinities near 5 g kg⁻¹ on the 29 July transect (Fig. 13b, d). In contrast, during downwelling on 3 July, thermohaline gradients were weaker, and the thermocline was deeper, centred around 20 m 610 (Fig. 13a, c). The different flow structure was noticeable. On 29 July, offshore flow was evident in the surface layer, particularly between 24.9° and 25.3°E (Fig. 13f, h). On 3 July, the current exhibited shoreward flow from the surface to 20 m depth, especially between 25.0° and 25.4°E (Fig. 13e, g). Both dates showed Ro O(1) near the topographic feature at ~25.0°E (Fig. 13k, I). The enhancement of spice near this location suggests that topographic features can trigger SMS instabilities and mixing, but SMS patches can travel offshore along slanted 615 isopycnals only when there is coastal topography persistently acts as a hotspot for SMS generation (Fig. 13m, n). However, under upwelling. Such conditions, these features become more dynamic and spatially extensive, amplifying thermohaline variability. Offshore Ro values remained generally low on 29 July (Fig. 131). Interestingly, a frontal zone was beginning to develop in the 25.15°-25.25°E region on 3 July (Fig. 13k), highlighting the localized and incipient character of SMS activity under downwelling conditions. Near this structure, vertical velocities were enhanced (Fig. 13i), and a modest increase in spice 620 was seen (Fig. 13m). On 29 July, vertical velocities were more spatially extensive and intensified above sloping topography (Fig. 13j), where enhanced interlayer exchange likely contributed to the observed spice. Spice were more intense and penetrated deeper into the water column on 29 July (Fig. 13n), reflecting both vertical and lateral redistribution of thermohaline

coastal and topographic irregularities. It can be noted that spice intensity is generally higher west from the largest peninsulas

properties, consistent with subduction and frontal advection. While meridional sections showed spice becoming more confined to the upper 15 m near the coast (Fig. 11g), the zonal transect revealed broader lateral displacement along the frontal zone.

This comparison of late July upwelling-related and early July downwelling conditions highlights how wind forcing and topography modulate SMS activity in the GoF. Both periods were governed by stable summer stratification, and recurrent SMS features were observed near topographic structures. However, the upwelling event on 29 July triggered sharper horizontal density gradients, stronger vertical shear, elevated Ro, and more extensive vertical velocities. These conditions favoured frontal instabilities, subduction, and lateral advection, resulting in deeper, more structured spice. In contrast, the downwelling regime on 3 July exhibited weaker gradients and more localized, surface-confined SMS subduction is directed against the secondary circulation at the mesoscale with offshore flow in the surface layer and onshore flow in the subsurface layer signals. Together, vertical sections and horizontal maps reveal how frontal processes and flow-topography interactions jointly control the intensity and extent of SMS variability.

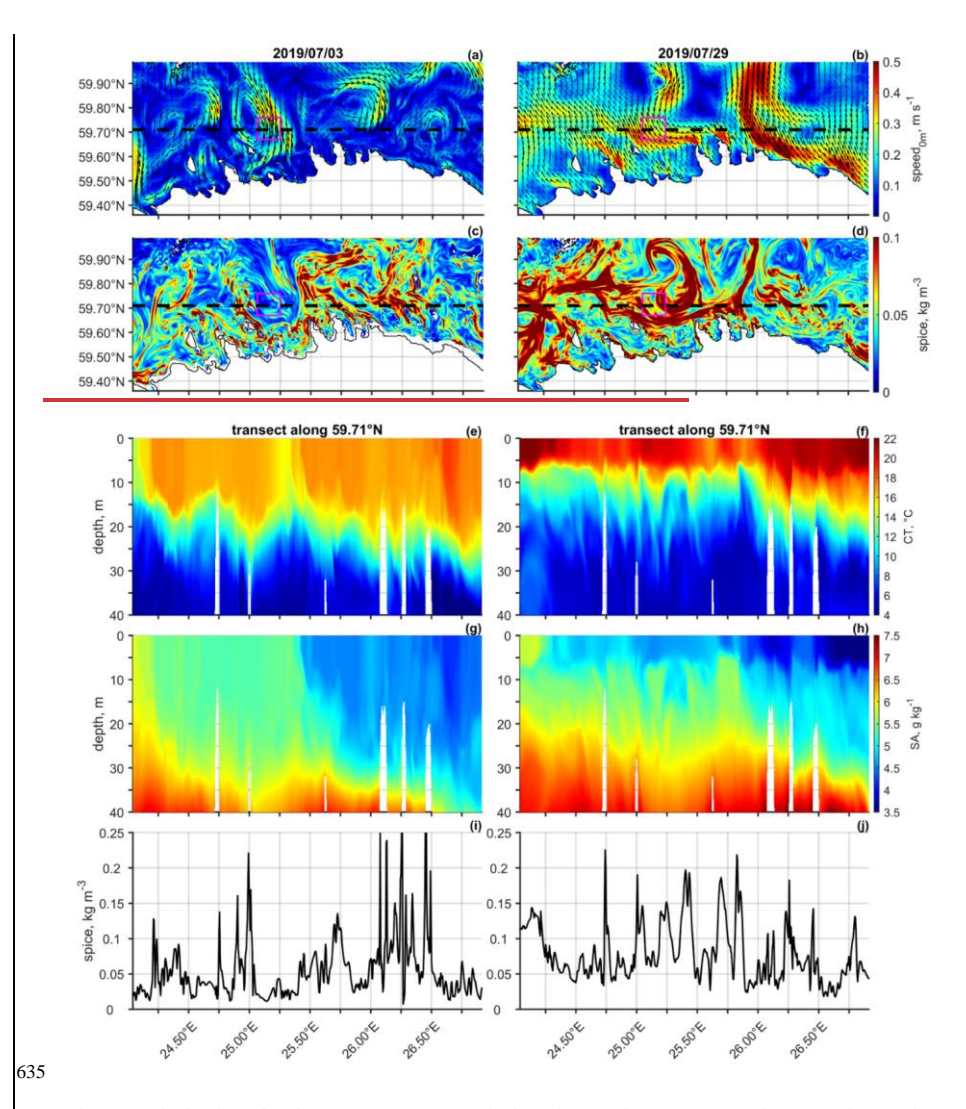


Figure 11. Distributions of surface currents (a,b) and spice intensity (c,d) in a larger area (with dashed line showing the location of section and the magenta box the 10×10 km study window) on 03.07.2019 (left column) and 29.07.2019 (right column). Vertical sections of temperature (e,f) and salinity (g,h), and graph of spice intensity (i,j) are shown along parallel 59.71° N.

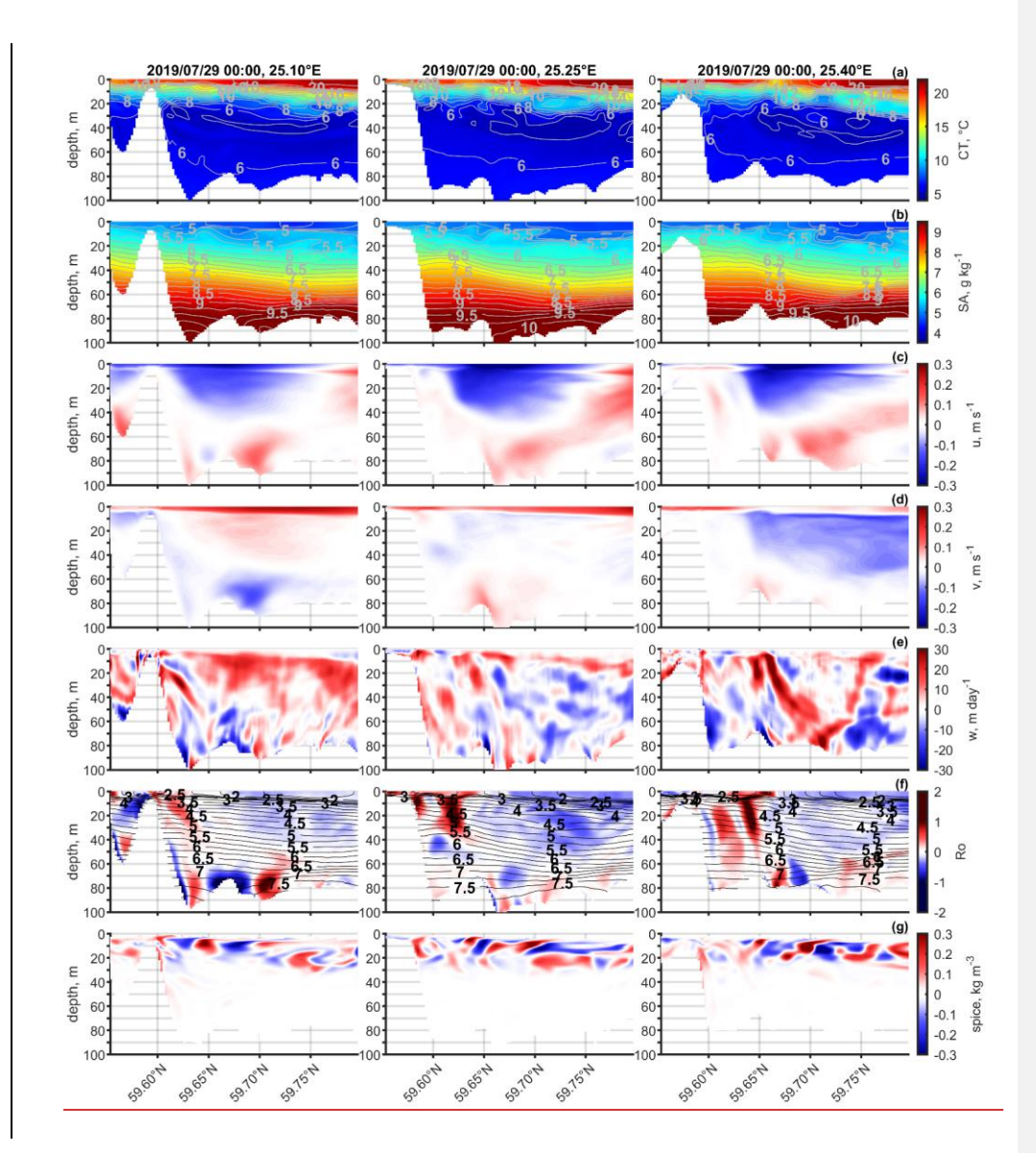
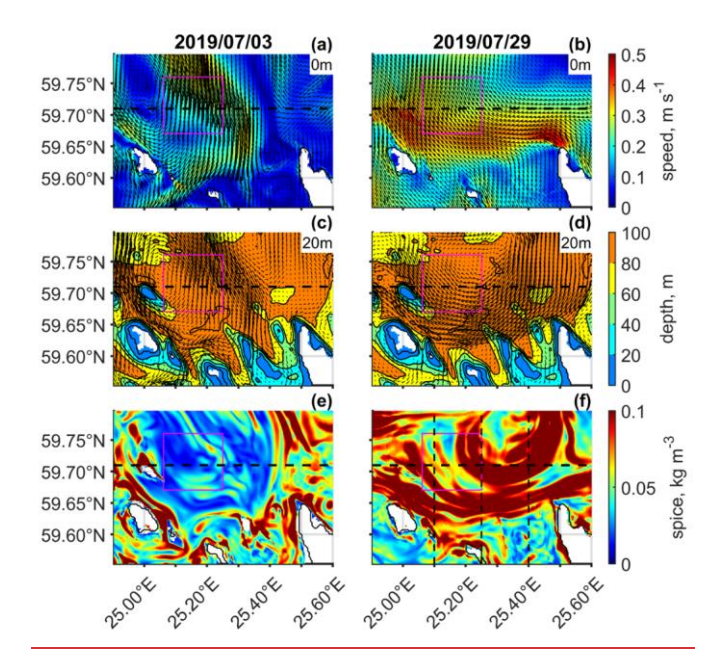


Figure 11: Vertical sections along three meridional transects at 25.10°E, 25.25°E, and 25.40°E on 29 July 2019, showing (a) Conservative Temperature (°C), (b) Absolute Salinity (kg kg ¹), (c) zonal velocity u (m s ¹), (d) meridional velocity v (m s ¹), (e) vertical velocity w (m dav ¹), (f) Rossby number (Ro) with overlaid isopvenals (0.25 kg m ³ intervals), and (g) spice (kg m ³). Transect locations are shown in Figure 12f.



650

645 Figure 12: Comparison of surface and subsurface conditions between 3 July (left column) and 29 July 2019 (right column). Panels a-b show surface horizontal velocity (m s-1), panels c-d velocity vectors at 20 m depth overlaid on bathymetry, and panels e-f root mean square of spice anomaly (kg m-3) in the density range limited from the surface to the depth of minimum temperature. The magenta box marks the 10×10 km study window. The horizontal black lines indicate the zonal transect shown in Figure 13. The vertical black lines in all panel f indicate the meridional transects shown in Figure 11.

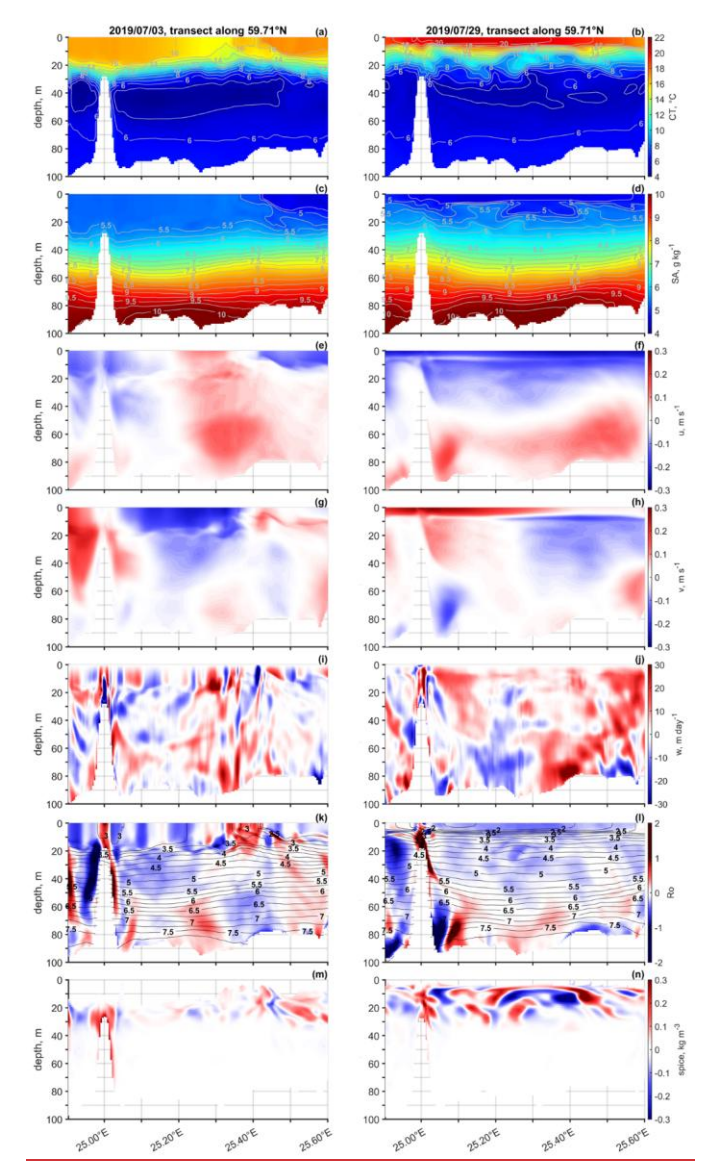


Figure 13: Vertical sections along zonal transects at 59.71° N on 3 July (left column) and 29 July 2019 (right column), showing (a-b) Conservative Temperature (°C), (c-d) Absolute Salinity (kg kg⁻¹), (e-f) zonal velocity u (m s⁻¹), (g-h) meridional velocity v (m s⁻¹), (i-j) vertical velocity w (m day⁻¹), (k-l) Rossby number (Ro) with overlaid isopycnals (0.25 kg m⁻³ intervals), and (m-n) spice (kg m⁻³).

4 Discussion

Despite the ubiquity of While satellite imagery has revealed widespread SMS variability onat the sea surface in the Baltic Sea observed via satellite images (e.g., Lavrova et al., 2018)), the vertical structure and their recognized implications for energy eascade (Naveira Garabato et al., 2022) and biogeochemistry (Mahadevan, 2016) in other marine systems, the dynamics and impacts of SMS processes are not widely explored in the Baltic Sea. Both numerical modelling and remain underexplored, particularly from observational studies confirm their occurrence during the upwelling (Lips et al., 2016a; Väli et al., 2017) and storm events (Carpenter et al., 2020; Chrysagi et al., 2021). Zhurbas et al. (2022) suggested the SMS processes in the UMLare separated from those in the layers below. Thedatasets. In this study, we built upon earlier glider-based observations analyzed by (Salm et al., (2023) confirm the presence of), which revealed subsurface SMS variability in and highlighted the subsurface layers, suggesting that thevalue of high-resolution autonomous measurements gathered. We extend this work by combining observational data with autonomous devices like gliders are essential for studying the SMS numerical simulations to examine the structure and variability of SMS features more comprehensively. This combined approach provides insight into the three-dimensional nature of SMS processes and enabled us to identify clear spice-based SMS signatures in the subsurface layers, co-located with regions of Ro O(1) and Ri<1 (Figs. 8a, d, e and 10), pointing to active SMS instability and mixing processes in the Baltic Sea. To our knowledge, this is the first study to apply this integrated approach to investigate SMS dynamics in the GoF.

The complex physical environment of the Baltic Sea is known to pose a challenge for numerical models, often resulting in biases in the simulated salinity and/or temperature fields, as well as inaccuracies in capturing the pycnoclines correctly (e.g., Gröger et al., 2022; Hordoir et al., 2019; Liblik et al., 2020; Väli et al., 2013). WeIn this study, we showed in the present study that the model with the SMS—permitting grid spacing could simulate the development of the vertical structure of the water column and the SMS variability reasonably well—the general spice variability exhibiting consistent patterns in both the measurements and the simulation. The general patterns of spice variability were consistent between measurements and simulation. The UML depth was also well captured, and the CIL was accurately reproduced during Missions I and III. However, during Mission II, the model underestimated the depth of the CIL by approximately 10 m and systematically underestimated the depth of the maximum N², with the largest discrepancy again occurring during Mission II (Fig. 5). Furthermore, the model did not capture the presence of occasionally observed two local maxima of N². These discrepancies could be related to difficulties in simulating salinity distributions in this basin (see, e.g., Westerlund et al., 2018). At the beginning of Mission I (spring 2018), the seasonal thermocline was almost absent (Fig. 3), and the salinity gradient defined the vertical density gradient. On the mentioned two occasions of two local N² maxima, the deeper one was largely determined

related to the large-scale advection and mixing of freshwater and saltier water) as accurately as temperature distributions (which are mostly defined by local atmospheric forcing). Similarly, Chrysagi et al. (2021) successfully compared the GETM simulation and the observations by replicating the structure of an observed cold SMS filament in the model. Studies in oceanic settings have demonstrated the pronounced influence of SMS processes on mixed layer depth (e.g., du Plessis et al., 2017). 690 This suggests that accurate simulation of SMS processes in the models could serve as a vital bridge for predicting the development of vertical stratification, coastal-offshore exchanges, etc. Despite these limitations, the model successfully captured the key SMS patterns and associated frontal structures, providing a reliable basis for interpreting the observed events and tracer distributions. Note, for instance, the identical vertical location of the highest spice intensity in relation to the UML depth and strongest density gradient in observations and model results (Fig. 695 6a-c). During spring missions, the spice maximum was situated at the base of the UML, but shallower than the strongest density gradient. During the summer mission, it was located just below the strongest density gradient. Similarly, Chrysagi et al. (2021) showed that a GETM simulation could replicate the structure of an observed cold SMS filament. To interpret the SMS structures, we employed spice as a tracer. Spice, which varies from cold and fresh to warm and salty, provides a dynamically passive tracer. We defined spice through along-isopycnal temperature and salinity anomalies with respect to the spatial mean considering typical internal Rossby deformation of 4 km. SomeWhile some studies have defined compute spice by analysing the whole dataset (across all spatial scales corresponding spatial scales) and have discussed to the dataset to examine the tracer spectra (spectral properties (e.g., Jaeger et al., 2020; Klymak et al., 2015). We propose that the), our scale-dependent spice well-definition emphasizes the SMS variability by revealing the patchy thermohaline structure around the features characterized by the order of one Rossby number and largenear regions of Ro O(1) 705 and elevated vertical velocities. Our analysis of spice intensity revealed that tracer patches captured in the vertical structure appear as elongated regions. These dimensions closely match estimations by Zhurbas et al. (2022), who suggested that the SMS structures are approximately 10-20 km in length and 1 km in width. Additionally, our simulation exhibited a small cyclonic vorticity within the study area in spring 2019, with spice following its periphery. Similar results by Yang et al. (2017), who observed heightened mixing in the eddy periphery, are consistent with the concept that the SMS flows provide a route for 710 energy toward smaller scales. (e.g., Fig. 11). The SMS tracer varianceSpice was consistently observed during all glider missions and throughout the modelling periods from May to August 2018 and 2019. Several observational studies have addressed the seasonal cycle of the SMS flows (e.g., Buckingham et al., 2016; Callies et al., 2015; Thompson et al., 2016). Thompson et al. (2016) demonstrated that the conditions favourable to the SMS instabilities vary throughout the year, with the SMS flows being more prevalent in the winter. The 715 seasonality in atmospheric forcing and stratification in the Baltic Sea would also suggest stronger SMS flows in winter than in spring summer, as simulated by Väli et al. (2024). Spice intensity, as it is defined in our study, reveals submesoscale flows only when both temperature and salinity contribute to density changes. For instance, in winter, when the sea surface temperature varies near the temperature of maximum density, salinity almost alone defines the water density, and the along-

by salinity, as detected by the glider. We suggest that the model does not simulate salinity distributions (which are mainly

isopycnal spice must be very low. It does not mean that the submesoscale flows do not exist; they do not leave this signature 720 in winter. It could explain an overall increasing trend in SMS intensities from spring to late summer with the warming up of tended to increase as the upper layer warmed and development of the seasonal thermocline but not the observed temporal peaks in spice intensity, developed. We argue that the observed spatial and temporal peaks in spice intensity, against the backdrop of an overall increasing trend, indicate the instances with high activity of SMS processes. Analysis of spice intensity revealed that tracer patches in the vertical structure appear as horizontally elongated features 725 (bottom rows in Figs. 10 and 12), closely matching the estimated dimensions of SMS structures (~10-20 km long, ~1 km wide) reported by Zhurbas et al. (2022). That study also suggested a vertical decoupling between SMS processes in the UML and those below. Our findings support this conceptual separation, showing that in summer months, SMS features frequently occurred below the UML (Fig. 6c), often decoupled from elevated surface Ro (Fig. 9). Furthermore, in early June 2019, the simulation showed a small cyclonic vorticity whose periphery was outlined by elevated 730 spice (Fig. 10b, e), consistent with observations by Yang et al. (2017), who linked such eddy peripheries with intensified mixing. These results indicate the potential of spice to reveal instances of SMS-driven energy transfer toward smaller scales. Recent studies have shown that surface heating can suppress SMS flows, and while surface cooling leads to more active SMS flows, but promotes them. However, favourable wind forcing can still enhance SMS activity also under surface heating conditions (Peng et al., 2021; Shang et al., 2023). On the other hand, when the wind forcing changes Changes or 735 reduces, reductions in wind forcing can also trigger SMS frontal instabilities can develop that result inlead to restratification of the UML, as shown by glider measurements and simulations in the Baltic Sea (Carpenter et al., 2020; Chrysagi et al., 2021; Salm et al., 2023). Horizontal The development of SMS flows depends critically on horizontal buoyancy gradients are essential for SMS development (e.g., Bosse et al., 2021; Ramachandran et al., 2018;), and which in GoF arise from multiple factors contribute to creating these gradients in the GoF sources (e.g., Lips et al., 2016a). The predominantly Predominantly positive 740 Q fosters water columnpromotes stratification in spring and early summer, although at different rates along their coastal and open sea areas (e.g., Lips et al., 2014). The Wind forcing influences the inclination of the thermocline depends on the wind forcing (Liblik and Lips, 2017), and occurrences of upwellings/downwellings while upwelling and downwelling events effectively form largestrong horizontal temperature, salinity and density gradients in spring-summer (e.g., Kikas and Lips, 2016). The SMS processes come into play gaining energy from created These lateral buoyancy gradients provide the energy 745 that drives SMS processes (Boccaletti et al., 2007). We suggest that the submesoscale SMS spice maxima observed above the maximum vertical density gradient in spring and in. under conditions of positive Q and lowweak wind forcing were signs of, reflect SMS processes acting to restratify the deeper portion of the UML. The secondary peakpeaks of spice intensity near the sea surface in June 2018 and August 2019 (Fig. 56e, g) could be relatedlinked to a characteristic forcing pattern fromduring these months - strong wind mixing events were followed by a period of weaker winds and positive Q. Thus, These results suggest that the submesoscales SMS processes can aetcontribute to restratify the UML-restratification both near the sea surface (under positive Q) and at its bottom, due to the base of the UML, driven by lateral buoyancy gradients, as also noted by Miracca-Lage et al. (2024). Oceanic studies have similarly demonstrated that SMS processes can strongly influence mixed layer depth (e.g., du Plessis et al., 2017), and our findings support this by showing that SMS processes (defined by spice-based signals) play a direct role in shaping the vertical stratification. This highlights the importance of resolving SMS variability in coastal models to improve predictions of stratification evolution and coastal—offshore exchanges.

755

760

765

770

775

780

785

CoolingConversely, cooling (negative Q) and wind-induced turbulence likely steer the dynamics within the UML, leading contribute to its the deepening of the UML. However, the SMS processes can also emerge below the UML and the maximum vertical density gradient, as was evidentobserved in July-August 2019, when both the windswind and Q were more variable. Dove et al. (2021) have shown reported that when the based eepening of the mixed layer deepened in regions of high eddy kinetic energy, a simultaneous increase in coincided with increased spice and oxygen concentration was observed concentrations below the mixed layer. Our In our data from, elevated subsurface spice in July-August 2019 showed that high spice intensity in the subsurface layer did not coincidealign with the elevated Ro at the sea surface at, but rather with the same site. Instead, presence of a baroclinic coastal current, varying in intensity and shape, was present nearby. We noted high relative vorticity. A particular example occurred at the end of July. The situation with Ro O(1) near the topographic features and surfacing of outcropping isopycnals, which were was characterized by high spice intensity in the offshore subsurface layer-(Fig. 11f, g) and intensification of vertical velocities, indicating SMS frontal subduction beneath the upwelling front (Fig. 11e). These signals, aligned with tilted isopycnals, indicate both vertical and lateral thermohaline displacement. The apparent decoupling between spice and Ro patterns likely reflects the downstream advection and transformation of SMS features beyond their generation sites, supporting a scenario of shallow subduction driven by persistent frontal tilting and vertical shear. Similar subduction along the slanted isopycnals associated with the submesoscaleSMS activity at the upwelling front has been reporteddescribed by Hosegood et al. (2017). Capo et al. (2023) further suggested that flow-topography interactions generate vorticities, which are transported offshore in the subsurface layers.

We showed that submesoscale variability in Our results from July 2019 highlight how coastal upwelling and downwelling regimes distinctly modulate SMS variability in the offshore subsurface layer differs between upwelling-(Figs. 12 and downwelling dominated background conditions. The winds 13). Winds favourable for the generation of upwelling (downwelling) in the southern GoF strengthen (weaken) vertical stratification and move the pycnocline upward (downward) towards the coast (Liblik and Lips, 2017). It could be suggested that coastal Coastal downwelling likely favours vertical turbulent mixing due to the weakening of by reducing vertical stratification, andmaking SMS features are less visible. Furthermore, if If SMS subduction occurs, the under these conditions, tracer patches are likely to be transported shoreward along the slanted isopycnals shoreward from beneath the downwelling-related baroclinic current. It explains why less intense SMS variability is observed offshore while it is high a similar localized intensification of spice near the topographic features (Fig. 11 left column).

Ruiz et al. (2019) showedunder upwelling- and downwelling-dominated conditions but with considerably weaker offshore SMS variability in the case of downwelling. This suggests that in a while topographic features consistently support SMS generation, upwelling enhances frontal subduction and the lateral spread of SMS structures into the basin's interior. Such

upwelling-related SMS subduction acts counter to the mesoscale front, 80% of the downward vertical flux of phytoplankton can be explained by the SMS subduction. It agrees with the observation of high phytoplankton biomass patches detected in connection to the submesoscale intrusions below the depth of the strongest vertical density gradient (Lips et al., 2011) and the accumulation of phytoplankton along the depressed isopycnals at the base of anti-cyclonic circulation cells in the GoF (Lips et al., 2010). Väli et al. (2024) revealed that the southern coastal area of the GoF is a region with the highest intensity of relative vorticity in the surface layer at the submesoscale in the Baltic Sea. Thus, the proposed SMS subduction process could feed transport and mixing in the offshore subsurface layer by exerting energy from unstable coastal currents over varying topography. These results accentuate the substantial role of SMS activity in the surface and subsurface layers of the Baltic Sea and its potential contribution to the vertical and coastal offshore transport of heat, salt, nutrients, oxygen, and carbon secondary circulation, which typically exhibits offshore surface flow and onshore subsurface return flow.

SMS subduction at fronts may contribute to the dissipation of mesoscale kinetic energy and downward transport of tracers (Archer et al., 2020), including the formation of subsurface chlorophyll maxima (e.g., Hofmann et al., 2024). By transporting phytoplankton-rich surface waters downward along sloping isopycnals, SMS processes can facilitate biomass accumulation below the pycnocline, as observed during summer in connection with anticyclonic circulation cells and SMS intrusions (Lips et al., 2010, 2011; Ruiz et al., 2019). Future analysis of collected glider data from the region, along with a comparison of spice variability with subsurface chlorophyll patchiness, could help to understand better the SMS processes and their biogeochemical impact in the Baltic Sea and similar stratified basins.

Conclusions

790

800

This study demonstrates that SMS variability in the Gulf of Finland is strongly modulated by both atmospheric forcing —
particularly surface heat flux and wind stress — and background hydrographic structures such as mesoscale frontal gradients.

Glider observations, supported by high-resolution modelling, revealed consistent spatial patterns of SMS activity, with SMS spice concentrated near the UML base in spring and within the thermocline in late summer, demonstrating the vertical sensitivity of SMS features to seasonal stratification. Wind forcing became dominant to shape the distribution of SMS anomalies when surface buoyancy input was weak. High SMS variability and subduction signatures were consistently found on the offshore side of a baroclinic coastal current, where sloped isopycnals aligned with velocity and SMS spice indicated downward and lateral transport of surface-layer waters. The integration of observations and model output allowed for extrapolation beyond individual glider transects, confirming that SMS processes in this coastal sea are both dynamically active and responsive to variations in external forcing. These results suggest the physical mechanisms that govern SMS variability and subduction in stratified coastal environments. Further studies, including high-resolution observations and modelling, are needed to understand SMS dynamics better and assess their biogeochemical consequences.

Code Availability Statement

Scripts to analyse the results are available upon request.

20 Data Availability Statement

The glider datasets analysed for this study can be found in online repository: doi:10.17882/96561 SEANOE. Model data is available upon request.

Author Contributions

KS was responsible for processing the glider data, analysing observational and model data and writing of the paper with contributions from GV, TL, and UL. UL contributed to the analysis setup and supervised the work. UL, TL, and KS participated in designing the surveys and piloting the glider. GV was responsible for the modelling activities.

Competing interests

The authors declare that they have no conflict of interest.

Acknowledgments

830 We would like to thank our colleagues and the crew of RV Salme for their assistance during the deployment and recovery of the glider. The computational resources from TalTech HPC are gratefully acknowledged. GETM community in Leibniz Institute for Baltic Sea Research (IOW) is gratefully acknowledged for maintaining and supporting the model code usage and development.

Funding

This work was supported by the Estonian Research Council grant (PRG602). The glider mission in the summer of 2019 was carried out as part of LAkHsMI (Sensors for LArge scale HydrodynaMic Imaging of ocean floor) project, which received funding from the European Union's Horizon 2020 Research and Innovation Programme grant No 635568.

References

Alenius, P., Nekrasov, A., and Myrberg, K.: Variability of the baroclinic Rossby radius in the Gulf of Finland, Cont. Shelf Res., 23 (6), 563–573, doi:10.1016/S0278-4343(03)00004-9, 2003.

- Archer, M., Schaeffer, A., Keating, S., Roughan, M., Holmes, R., & Siegelman, L.: Observations of submesoscale variability and frontal subduction within the mesoscale eddy field of the Tasman Sea, J. Phys. Oceanogr., 50(5), 1509–1529, doi:10.1175/JPO-D-19-0131.1, 2020.
- Boccaletti, G., Ferrari, R., and Fox-Kemper, B.: Mixed layer instabilities and restratification, J. Phys. Oceanogr., 37 (9), 2228–2250, doi:10.1175/JPO3101.1, 2007.
- Bosse, A., Testor, P., Damien, P., Estournel, C., Marsaleix, P., Mortier, L., Prieur, L., and Taillandier, V.: Wind-forced submesoscale symmetric instability around deep convection in the Northwestern Mediterranean Sea, Fluids, 6(3), 123, doi:10.3390/fluids6030123, 2021.
- Buckingham, C. E., Naveira Garabato, A. C., Thompson, A. F., Brannigan, L., Lazar, A., Marshall, D. P., George Nurser, A.
 J., Damerell, G., Heywood, K. J., and Belcher, S. E.: Seasonality of submesoscale flows in the ocean surface boundary layer,
 Geophys. Res. Lett., 43(5), 2118–2126, doi:10.1002/2016GL068009, 2016.
 - Burchard, H., and Bolding, K.: Comparative analysis of four second-moment turbulence closure models for the oceanic mixed layer, J. Phys. Oceanogr., 31(8), 1943–1968, doi:10.1175/1520-0485(2001)031<1943:CAOFSM>2.0.CO;2, 2001.
- Burchard, H., and Bolding, K.: GETM a general estuarine transport model. Scientific Documentation, Tech. Rep., EUR 20253 EN, 2002.
 - Callies, J., Ferrari, R., Klymak, J. M., and Gula, J.: Seasonality in submesoscale turbulence, Nat. Commun., 6, doi:10.1038/ncomms7862, 2015.
 - Canuto, V. M., Howard, A., Cheng, Y., and Dubovikov, M. S.: Ocean turbulence. Part I: One-point closure model-momentum and heat vertical diffusivities, J. Phys. Oceanogr., 31(6), 1413–1426, doi:10.1175/1520-0485(2001)031<1413:OTPIOP>2.0.CO; 2.2001.

860

doi:10.1029/2020GL090365, 2020.

- Capo, E., McWilliams, J. C., and Jagannathan, A.: Flow-topography interaction along the Spanish slope in the Alboran Sea:

 Vorticity generation and connection to interior fronts, J. Geophys. Res.: Oceans, 128, e2022JC019480, doi:10.1029/2022JC019480, 2023.
- Capet, X., McWilliams, J. C., Molemaker, M. J., and Shchepetkin, A. F.: Mesoscale to submesoscale transition in the California
 Current system. Part III: Energy balance and flux, J. Phys. Oceanogr., 38(10), 2256–2269, doi:10.1175/2008JPO3810.1, 2008.
 Carpenter, J. R., Rodrigues, A., Schultze, L. K. P., Merckelbach, L. M., Suzuki, N., Baschek, B., and Umlauf, L.: Shear instability and turbulence within a submesoscale front following a storm, Geophys. Res. Lett., 47(23),
 - Chrysagi, E., Umlauf, L., Holtermann, P., Klingbeil, K., and Burchard, H.: High-resolution simulations of submesoscale processes in the Baltic Sea: The role of storm events, J. Geophys. Res.: Oceans, 126(3), doi:10.1029/2020JC016411, 2021.
- Dove, L. A., Thompson, A. F., Balwada, D., and Gray, A. R.: Observational evidence of ventilation hotspots in the Southern Ocean, J. Geophys. Res.: Oceans, 126(7), doi:10.1029/2021JC017178, 2021.
 - du Plessis, M., Swart, S., Ansorge, I. J., and Mahadevan, A.: Submesoscale processes promote seasonal restratification in the Subantarctic Ocean, J. Geophys. Res.: Oceans, 122(4), 2960–2975, doi:10.1002/2016JC012494, 2017.

- 875 Elken, J., Nõmm, M., Lagemaa, P.: Circulation patterns in the Gulf of Finland derived from the EOF analysis of model results, Boreal Environment Research, 16, 84–102, 2011.
 - Gräwe, U., Holtermann, P., Klingbeil, K., and Burchard, H.: Advantages of vertically adaptive coordinates in numerical models of stratified shelf seas, Ocean Modelling, 92, 56–68, doi:10.1016/j.ocemod.2015.05.008, 2015.
 - Gröger, M., Placke, M., Meier, H. E. M., Börgel, F., Brunnabend, S. E., Dutheil, C., Gräwe, U., Hieronymus, M., Neumann,
- 880 T., Radtke, H., Schimanke, S., Su, J., and Väli, G.: The Baltic Sea Model Intercomparison Project (BMIP) a platform for model development, evaluation, and uncertainty assessment, Geosci. Model Dev., 15(22), 8613–8638, doi:10.5194/gmd-15-8613-2022, 2022.
 - Hersbach, H., Bell, B., Berrisford, P., Hirahara, S., Horányi, A., Muñoz-Sabater, J., Nicolas, J., Peubey, C., Radu, R., Schepers, D., Simmons, A., Soci, C., Abdalla, S., Abellan, X., Balsamo, G., Bechtold, P., Biavati, G., Bidlot, J., Bonavita, M., ...
- 885 Thépaut, J. N.: The ERA5 global reanalysis. Quarterly Journal of the Royal Meteorological Society, 146(730), 1999–2049, doi:10.1002/qj.3803, 2020.
 - Hofmann, Z., von Appen, W.-J., Kanzow, T., Becker, H., Hagemann, J., Hufnagel, L., and Iversen, M. H.: Stepwise subduction observed at a front in the marginal ice zone in Fram Strait, J. <u>Geophys. Res.</u>: Oceans, 129, e2023JC020641, doi:10.1029/2023JC020641, 2024.
- 890 Hofmeister, R., Burchard, H., and Beckers, J. M.: Non-uniform adaptive vertical grids for 3D numerical ocean models, Ocean Modelling, 33(1–2), 70–86, doi:10.1016/j.ocemod.2009.12.003, 2010.

Geosci. Model Dev., 12(1), 363-386, doi:10.5194/gmd-12-363-2019, 2019.

- Hordoir, R., Axell, L., Höglund, A., Dieterich, C., Fransner, F., Gröger, M., Liu, Y., Pemberton, P., Schimanke, S., Andersson, H., Ljungemyr, P., Nygren, P., Falahat, S., Nord, A., Jönsson, A., Lake, I., Döös, K., Hieronymus, M., Dietze, H., ... Haapala, J.: Nemo-Nordic 1.0: A NEMO-based ocean model for the Baltic and North seas Research and operational applications,
- Hosegood, P. J., Nightingale, P. D., Rees, A. P., Widdicombe, C. E., Woodward, E. M. S., Clark, D. R., and Torres, R. J.: Nutrient pumping by submesoscale circulations in the mauritanian upwelling system, Progress in Oceanography, 159, 223–236, doi:10.1016/j.pocean.2017.10.004, 2017.
- Jaeger, G. S., Mackinnon, J. A., Lucas, A. J., Shroyer, E., Nash, J., Tandon, A., Farrar, J. T., and Mahadevan, A.: How spice is stirred in the Bay of Bengal, J. Phys. Oceanogr., 50(9), 2669–2688, doi:10.1175/JPO-D-19-0077.s1, 2020.
 - Janssen, F., Schrum, C., and Backhaus, J. O.: A climatological data set of temperature and salinity for the Baltic Sea and the North Sea, Deutsche Hydrographische Zeitschrift, 51(9), 5, doi:10.1007/BF02933676, 1999.
 - Jhugroo, K., O'Callaghan, J., Stevens, C. L., Macdonald, H. S., Elliott, F., and Hadfield, M. G.: Spatial Structure of Low Salinity Submesoscale Features and Their Interactions With a Coastal Current, Front. Mar. Sci., 7, 557360, doi: 10.3389/fmars.2020.557360, 2020.
 - Kikas, V., and Lips, U.: Upwelling characteristics in the Gulf of Finland (Baltic Sea) as revealed by Ferrybox measurements in 2007-2013, Ocean Sci., 12(3), 843–859, doi:10.5194/os-12-843-2016, 2016.

- Klingbeil, K., Lemarié, F., Debreu, L., and Burchard, H.: The numerics of hydrostatic structured-grid coastal ocean models: State of the art and future perspectives, Ocean Modelling, 125, 80–105, doi:10.1016/j.ocemod.2018.01.007, 2018.
- 910 Klymak, J. M., Crawford, W., Alford, M. H., Mackinnon, J. A., and Pinkel, R.: Along-isopycnal variability of spice in the North Pacific, J. Geophys. Res.: Oceans, 120(3), 2287–2307, doi:10.1002/2013JC009421, 2015.
 - Kondo, J.: Air-sea bulk transfer coefficients in diabatic conditions, Boundary-Layer Meteorology, 9, 91–112, doi:10.1007/BF00232256.1975.
- Krauss, W., and Brügge, B.: Wind-produced water exchange between the deep basins of the Baltic Sea, J. Phys. Oceanogr., 915 21(3), 373–384. doi:10.1175/1520-0485(1991)021<0373:WPWEBT>2.0.CO:2, 1991.
 - Lavrova, O. Y., Krayushkin, E. V., Strochkov, A. Ya., and Nazirova, K. R.: Vortex structures in the Southeastern Baltic Sea: satellite observations and concurrent measurements, Proceedings Volume 10784, Remote Sensing of the Ocean, Sea Ice, Coastal Waters, and Large Water Regions 2018, 1078404, doi:10.1117/12.2325463, 2018.
- Lehmann, A., Myrberg, K., and Höflich, K.: A statistical approach to coastal upwelling in the Baltic Sea based on the analysis of satellite data for 1990-2009, Oceanologia, 54(3), 369–393, doi:10.5697/oc.54-3.369, 2012.
 - Liblik, T., and Lips, U.: Variability of pycnoclines in a three-layer, large estuary: the Gulf of Finland, Boreal Environment Research, 22, 27–47, 2017.
 - Liblik, T., Väli, G., Lips, I., Lilover, M. J., Kikas, V., and Laanemets, J.: The winter stratification phenomenon and its consequences in the Gulf of Finland, Baltic Sea, Ocean Sci., 16(6), 1475–1490, doi:10.5194/os-16-1475-2020, 2020.
- 925 Liblik, T., Väli, G., Salm, K., Laanemets, J., Lilover, M. J., and Lips, U.: Quasi-steady circulation regimes in the Baltic Sea, Ocean Sci., 18(3), 857–879, doi:10.5194/os-18-857-2022, 2022.
 - Lilover, M. J., Elken, J., Suhhova, I., and Liblik, T.: Observed flow variability along the thalweg, and on the coastal slopes of the Gulf of Finland, Baltic Sea, Estuarine, Coastal and Shelf Science, 195, 23–33, doi:10.1016/j.ecss.2016.11.002, 2017.
 - Lindström, G., Pers, C., Rosberg, J., Strömqvist, J., and Arheimer, B.: Development and testing of the HYPE (Hydrological
- 930 Predictions for the Environment) water quality model for different spatial scales, Hydrology Research, 41(3-4), 295-319, doi:10.2166/nh.2010.007, 2010.
 - Lips, I., Lips, U., and Liblik, T: Consequences of coastal upwelling events on physical and chemical patterns in the central Gulf of Finland (Baltic Sea), Cont. Shelf Res., 29, 1836–1847, doi:10.1016/j.csr.2009.06.010, 2009.
 - Lips, U., Lips, I., Liblik, T., Kikas, V., Altoja, K., Buhhalko, N., and Rünk, N.: Vertical dynamics of summer phytoplankton in a stratified estuary (Gulf of Finland, Baltic Sea), Ocean Dyn., 61, 903–915, doi:10.1007/s10236-011-0421-8, 2011.
 - Lips, U., Kikas, V., Liblik, T., and Lips, I.: Multi-sensor in situ observations to resolve the sub-mesoscale features in the stratified Gulf of Finland, Baltic Sea, Ocean Sci., 12(3), 715–732, doi:10.5194/os-12-715-2016, 2016a.
 - Lips, U., Laanemets, J., Lips, I., Liblik, T., Suhhova, I., and <u>Suursaarsonaar</u>, Ü.: Wind-driven residual circulation and related oxygen and nutrient dynamics in the Gulf of Finland (Baltic Sea) in winter, Estuarine, Coastal and Shelf Science, 195, 4–15, doi:10.1016/j.ecss.2016.10.006, 2017.

Formatted: Swedish (Sweden)

- Lips, U., Lips, I., Liblik, T., and Kuvaldina, N.: Processes responsible for the formation and maintenance of sub-surface chlorophyll maxima in the Gulf of Finland, Estuarine, Coastal and Shelf Science, 88, 339–349, doi:10.1016/j.ecss.2010.04.015, 2010.
- Lips, I., Rünk, N., Kikas, V., Meerits, A., and Lips, U.: High-resolution dynamics of the spring bloom in the Gulf of Finland of the Baltic Sea, J. Mar. Syst., 129, 135–149, doi:10.1016/j.jmarsys.2013.06.002, 2014.
 - Lips, U., Zhurbas, V., Skudra, M., and Väli, G.: A numerical study of circulation in the Gulf of Riga, Baltic Sea. Part I: Whole-basin gyres and mean currents, Cont. Shelf Res., 112, 1–13, doi:10.1016/j.csr.2015.11.008, 2016b.
 - Mahadevan, A.: The impact of submesoscale physics on primary productivity of plankton, Annual Review of Marine Science, 8, 161–184, doi:10.1146/annurev-marine-010814-015912, 2016.
- McDougall T., and Barker P. M.: Getting started with TEOS-10 and the Gibbs Seawater (GSW) Oceanographic Toolbox, 28pp., SCOR/IAPSO WG127, ISBN 978-0-646-55621-5, available at: https://www.teos-10.org/software.htm, 2011
 - Miracca-Lage, M., Becherer, J., Merckelbach, L., Bosse, A., Testor, P., and Carpenter, J. R.: Rapid restratification processes control mixed layer turbulence and phytoplankton growth in a deep convection region, Geophys. Res. Lett., 51, e2023GL107336, doi:10.1029/2023GL107336, 2024.
- 955 Naveira Garabato, A. C., Yu, X., Callies, J., Barkan, R., Polzin, K. L., Frajka-Williams, E. E., Buckingham, C. E., and Griffies, S. M.: Kinetic energy transfers between mesoscale and submesoscale motions in the open ocean's upper layers, J. Phys. Oceanogr., 52(1), 75–97, doi:10.1175/JPO-D-21-0099.1, 2022.
 - Peng, J.-P., Dräger-Dietel, J., North, R. P., and Umlauf, L.: Diurnal variability of frontal dynamics, instability, and turbulence in a submesoscale upwelling filament, J. Phys. Oceanogr., 51(9), 2825–2843, doi:10.1175/JPO-D-21-0033.1, 2021.
- 960 Ramachandran, S., Tandon, A., Mackinnon, J., Lucas, A. J., Pinkel, R., Waterhouse, A. F., Nash, J., Shroyer, E., Mahadevan, A., Weller, R. A., and Farrar, J. T.: Submesoscale processes at shallow salinity fronts in the Bay of Bengal: Observations during the winter monsoon, J. Phys. Oceanogr., 48(3), 479–509, doi:10.1175/JPO-D-16-0283.1, 2018.
 - Reissmann, J. H., Burchard, H., Feistel, R., Hagen, E., Lass, H. U., Mohrholz, V., Nausch, G., Umlauf, L., and Wieczorek, G.: Vertical mixing in the Baltic Sea and consequences for eutrophication—A review, In Progress in Oceanography, 82 (1), 47—80, doi:10.1016/j.pocean.2007.10.004, 2009.
 - Rudnick, D. L., and Cole, S. T.: On sampling the ocean using underwater gliders, J. Geophys. Res.: Oceans, 116(8), doi:10.1029/2010JC006849, 2011.
 - Rudnick, D. L., and Ferrari, R.: Compensation of horizontal temperature and salinity gradients in the ocean mixed layer, Science, 283(5401), 526–529, doi:10.1126/science.283.5401.526, 1999.
- 970 Ruiz, S., Claret, M., Pascual, A., Olita, A., Troupin, C., Capet, A., Tovar-Sánchez, A., Allen, J., Poulain, P.-M., Tintoré, J., and Mahadevan, A.: Effects of oceanic mesoscale and submesoscale frontal processes on the vertical transport of phytoplankton, J. Geophys. Res.: Oceans, 124, 5999–6014, doi:10.1029/2019JC015034, 2019.
 - Salm, K., Liblik, T., and Lips, U.: Submesoscale variability in a mesoscale front captured by a glider mission in the Gulf of Finland, Baltic Sea, Front. Mar. Sci., 10, doi:10.3389/fmars.2023.984246, 2023.

Formatted: English (United Kingdom)

- 975 Shang, X., Shu, Y., Wang, D., Yu, J., Mao, H., Liu, D., Qiu, C., and Tang, H.: Submesoscale motions driven by down-front wind around an anticyclonic eddy with a cold core, J. Geophys. Res.: Oceans, 128(8), doi:10.1029/2022JC019173, 2023.
 Siht, E., Väli, G., Liblik, T., Mishra, A., Buhhalko, N., and Lips, U.: Modeling the pathways of microplastics in the Gulf of Finland, Baltic Sea sensitivity of parametrizations, Ocean Dyn., in press 2025.
- Suursaar, Ü_{7.2} and Aps, R.: Spatio-temporal variations in hydro-physical and -chemical parameters during a major upwelling event off the southern coast of the Gulf of Finland in summer 2006, Oceanologia, 49 (2), 209–228, 2007.
 - Taylor, J. R., and Thompson, A. F.: Submesoscale dynamics in the upper ocean, Annu. Rev. Fluid Mech., 55(1), 103–127, doi:10.1146/annurev-fluid-031422, 2023.
 - Tarry, D. R., Ruiz, S., Johnston, T. M. S., Poulain, P.-M., Özgökmen, T., Centurioni, L. R., et al.: Drifter observations reveal intense vertical velocity in a surface ocean front, Geophys. Res. Lett., 49, e2022GL098969, doi:10.1029/2022GL098969, 2022.
- 785 Thomas, L. N., Tandon, A., and Mahadevan, A.: Submesoscale processes and dynamics, Geophys. Monogr. Ser., 177, 17–38, doi:10.1029/177GM04, 2008.
 - Thompson, A. F., Lazar, A., Buckingham, C., Garabato, A. C. N., Damerell, G. M., and Heywood, K. J.: Open ocean submesoscale motions: A full seasonal cycle of mixed layer instabilities from gliders, J. Phys. Oceanogr., 46(4), 1285–1307, doi:10.1175/JPO-D-15-0170.1, 2016.
- 990 Uiboupin, R. and Laanemets, J.: Upwelling characteristics derived from satellite sea surface temperature data in the Gulf of Finland, Baltic Sea, Boreal Environment Research, 14 (2), 297–304, 2009.
 - Umlauf, L., and Burchard, H.: Second-order turbulence closure models for geophysical boundary layers. A review of recent work, Cont. Shelf Res., 25, 795–827, doi:10.1016/j.csr.2004.08.004, 2005.
 - Väli, G., Meier, H. E. M., and Elken, J.: Simulated halocline variability in the baltic sea and its impact on hypoxia during 1961-2007, J. Geophys. Res.: Oceans, 118(12), 6982–7000, doi:10.1002/2013JC009192, 2013.
 - Väli, G., Meier, H.E.M., Liblik, T., Radtke, H., Klingbeil, K., Gräwe, U., and Lips, U.: Submesoscale processes in the surface layer of the central Baltic Sea: A high-resolution modelling study, Oceanologia, 66 (1), 78–90, doi: 10.1016/j.oceano.2023.11.002, 2024.
- Väli, G., Meier, H. E. M., Placke, M., and Dieterich, C.: River runoff forcing for ocean modeling within the Baltic Sea Model

 1000 Intercomparison Project, Marine Science Reports, 113, doi:10.12754/msr-2019-0113, 2019.
 - Väli, G., Zhurbas, V., Lips, U., and Laanemets, J.: Submesoscale structures related to upwelling events in the Gulf of Finland, Baltic Sea (numerical experiments), J. Mar. Syst., 171, 31–42, doi:10.1016/j.jmarsys.2016.06.010, 2017.
 - Westerlund, A., Tuomi, L., Alenius, P., Miettunen, E., Vankevich, R.E.: Attributing mean circulation patterns to physical phenomena in the Gulf of Finland, Oceanologia, 60(1), 16-31, doi:10.1016/j.oceano.2017.05.003, 2018.
- Westerlund, A., Tuomi, L., Alenius, P., Myrberg, K., Miettunen, E., Vankevich, R. E., and Hordoir, R.: Circulation patterns in the Gulf of Finland from daily to seasonal timescales, Tellus A: Dynamic Meteorology and Oceanography, 71(1), doi:10.1080/16000870.2019.1627149, 2019.

Formatted: English (United Kingdom)

Wong, A., Keeley, R., Carval, T., and the Argo Data Management Team: Argo Quality Control Manual for CTD and Trajectory Data, doi:10.13155/33951, 2025.

1010 Yang, Q., Zhao, W., Liang, X., Dong, J., and Tian, J.: Elevated mixing in the periphery of mesoscale eddies in the South China Sea, J. Phys. Oceanogr., 47(4), 895–907, doi:10.1175/JPO-D-16-0256.1, 2017.

Zhurbas, V., Väli, G., Golenko, M., and Paka, V.: Variability of bottom friction velocity along the inflow water pathway in the Baltic Sea, J. Mar. Syst., 184, 50–58, doi:10.1016/j.jmarsys.2018.04.008, 2018.

Zhurbas, V., Väli, G., and Kuzmina, N.: Striped texture of submesoscale fields in the northeastern Baltic Proper: Results of very high-resolution modelling for summer season, Oceanologia, 64(1), 1–21, doi:10.1016/j.oceano.2021.08.003, 2022.

53